

## APPROXIMATE INFERENCE FOR CONSTRUCTING ASTRONOMICAL CATALOGS FROM IMAGES

BY JEFFREY REGIER<sup>1</sup>, ANDREW C. MILLER<sup>2</sup>, DAVID SCHLEGEL<sup>3</sup>,  
RYAN P. ADAMS<sup>4,5</sup>, JON D. MCAULIFFE<sup>1,6</sup>, AND PRABHAT<sup>3</sup>

*University of California, Berkeley<sup>1</sup>, Harvard University<sup>2</sup>,  
Lawrence Berkeley National Laboratory<sup>3</sup>, Google Brain<sup>4</sup>,  
Princeton University<sup>5</sup>, and The Voleon Group<sup>6</sup>.*

We present a new, fully generative model for constructing astronomical catalogs from optical telescope image sets. Each pixel intensity is treated as a Poisson random variable with a rate parameter that depends on the latent properties of stars and galaxies. These latent properties are themselves random, with prior distributions fitted by empirical Bayes. We compare two procedures for posterior inference. One procedure is based on Markov chain Monte Carlo (MCMC) while the other is based on variational inference (VI). We demonstrate that the MCMC procedure excels at quantifying uncertainty while the VI procedure is  $1000\times$  faster. For the error metric we consider, both procedures outperform the current state-of-the-art method for measuring the colors, shapes, and morphologies of stars and galaxies. On a supercomputer, the VI procedure efficiently uses 665,000 CPU cores (1.3 million hardware threads) to construct an astronomical catalog from 50 terabytes of images.

---

*MSC 2010 subject classifications:* Primary 62P35; secondary 85A35

*Keywords and phrases:* astronomy, graphical model, MCMC, variational inference, high performance computing

**1. Introduction.** Astronomical surveys are the primary source of information about the universe beyond our solar system. They are essential for addressing key open questions in astronomy and cosmology about topics such as the life cycles of stars and galaxies, the nature of dark energy, and the origin and evolution of the universe.

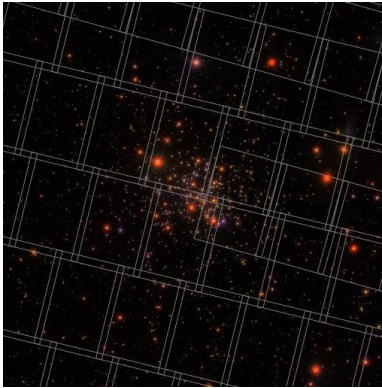


Fig 1: Sample data from the Sloan Digital Sky Survey (SDSS). Image boundaries appear as grey lines. All images have the same rectangular size; there is overlap.

The principal products of astronomical imaging surveys are catalogs of light sources, such as stars and galaxies. These catalogs are generated by identifying light sources in survey images (e.g., Figure 1) and characterizing each according to physical parameters such as flux<sup>1</sup>, color, and morphology.

Astronomical catalogs are the starting point for many scientific analyses. First, catalogs assist with discovering new types of astronomical objects, such as new populations of stars or galaxies, or entirely new objects. The catalog can either resolve the research question directly, or it may serve to inform the design of follow-on surveys using more advanced or specialized instrumentation. Second, catalogs enable demographic inference, which can address fundamental cosmological questions. For example, researchers may need to know the spatial and luminosity distributions for specific classes of stars or galaxies. For these “population-level” analyses, accurate quantification of uncertainty in the point estimates of parameters is as important as the accuracy of the point estimates themselves.

Catalog construction today is based on software pipelines. For concreteness, we describe the Hyper Suprime-Cam (HSC) software pipeline (Bosch et al. 2018). The contrasts we subsequently draw between our proposed ap-

---

<sup>1</sup>Flux is the amount of energy transferred in the form of photons at a certain distance from the source per unit area per second. “Brightness” is a colloquial term for flux.

proach and HSC, however, apply to catalog pipelines in general. We focus on HSC because it is the state of the art in nearly all respects. Its code has been merged into the cataloging pipeline for the Large Synoptic Survey Telescope (LSST 2017)—one of the most important upcoming sky surveys. HSC draws upon the algorithmic development of both the Sloan Digital Sky Survey (SDSS) software pipeline (Lupton et al. 2001) and SExtractor (Bertin & Arnouts 1996).

The HSC software pipeline comprises a sequence of steps, including 1) detrending, 2) cosmic ray masking, 3) “repair” of saturated and bad pixels through interpolation, 4) estimating the sky background, 5) detecting “peaks”, 6) estimating the centroids of light sources, 7) estimating the shape of light sources, 8) estimating the flux of light sources, 9) matching light sources to external catalogs, 10) estimating the point-spread function, and 11) performing star/galaxy separation. Most of these steps depend on estimates from other steps, and many have circular dependencies. Steps with circular dependencies are repeated multiple times. For example, at first a circular Gaussian serves as a crude approximation of a star for masking cosmic rays. Later the cosmic ray detector is rerun with a refined star model.

For the initial sequence of steps (i.e., a “stage”), the semi-iterative sequence steps are executed on all images independently, regardless of any overlap. During later stages, constraints are added that require the algorithm to use a shared estimate for a light source in an overlapping region. The matching itself depends on aligning the images correctly, which in turn depends on correctly detected light sources—an additional circular dependency. Ultimately, aligned, calibrated, and deblended images are “co-added” (superimposed) to create one image for each light source. The final estimate of a light source’s properties is based on the co-added images and accompanying per-pixel variance estimates.

The uncertainty estimates for a light source’s flux include only this pixel-level variability. They do not account for all the other sources of uncertainty that cannot reasonably be modeled as independent across pixels: uncertainty about the light source’s centroid, the number of light sources, the image alignments, cosmic ray detection, light sources’ shapes, and nearby light sources’ fluxes and shapes. The reported uncertainties are based on a Gaussian statistical model of pixels, but one that conditions on the previous stages’ estimates of all these quantities. Effectively, the reported uncertainties are for a conditional distribution rather than a marginal distribution.

Modern cataloging pipelines have struck a balance between algorithmic efficiency and statistical rigor that has enabled much of the progress in astronomy to date. Upcoming surveys, however, will probe deeper into the visible universe, creating new challenges. In particular, whereas blending was

thought to affect just a small number of light sources, in LSST, it is estimated that 68% of light sources will be blended, requiring new approaches to deblending (Bosch et al. 2018). In addition, new approaches may let us better interpret existing survey data. Our aim in this work is to put catalog construction on sounder statistical footing.

Our first contribution is a statistical model (Section 2) that can simultaneously find centroids, determine photometry (flux, color, and galaxy morphology), deblend overlapping light sources, perform star/galaxy separation, and adjust estimates of all quantities based on prior information. Our procedure for all these tasks is based on a single probabilistic model. The properties of cataloged light sources are modeled as unobserved random variables. The number of photons recorded by each pixel is modeled by a Poisson distribution with a rate parameter unique to the pixel. The posterior distribution induced over the unobserved physical properties of the light sources encapsulates knowledge about the catalog’s entries, combining prior knowledge of astrophysics with survey imaging data in a statistically efficient manner. With the model, we can reason about uncertainty for any quantity in our catalog without conditioning on other estimates being known exactly.

Unfortunately, exact Bayesian posterior inference is NP-hard for most probabilistic models of interest (Bishop 2006), including this one. Approximate Bayesian inference is an area of active research. Markov chain Monte Carlo (MCMC) is the most common approach. Two recent studies demonstrate that Bayesian modeling is the gold standard for astronomical inference, while casting doubt on whether MCMC is viable for constructing a whole astronomical catalog. Brewer et al. (2013) use a single 10,000-pixel image as the dataset for an MCMC procedure. Obtaining samples from the posterior distribution takes one day using a modern multi-core computer. Portillo et al. (2017) run twelve Intel Xeon cores for an entire day to yield useful results on a similar dataset. The Sloan Digital Sky Survey—a modern astronomical survey—contains over a billion times as many pixels as these test images. The upcoming Large Synoptic Survey Telescope (LSST) will collect at least ten terabytes nightly—hundreds of petabytes in total (LSST 2017). Even basic management of this data requires substantial engineering effort.

Before our work, Tractor (Lang et al. 2016) was the only program for Bayesian posterior inference that had been applied to a complete modern astronomical imaging survey. Tractor is an unpublished work. It relies on the Laplace approximation: the posterior is approximated by a multivariate Gaussian distribution centered at the mode, having a covariance matrix equal to the negative Hessian of the log-likelihood function at that mode. This approximation is not suitable for either categorical random variables or random variables with multi-modal posteriors—no Gaussian distribution ap-

proximates them well. Additionally, because Laplace approximation centers the Gaussian at the mode of the target, rather than the mean, the solution depends on the problem parameterization (Bishop 2006).

Variational inference (VI) is an alternative to MCMC and the Laplace approximation. Like the latter, it uses numerical optimization, not sampling, to find a distribution that approximates the posterior (Blei et al. 2017). In practice, the resulting optimization problem is often orders of magnitude faster to solve compared to MCMC approaches. It can be simpler, too. Whereas MCMC transition operators must satisfy strict constraints for validity, the variational optimization problem can in principle be solved using any off-the-shelf technique for numerical optimization. Scaling VI to large datasets is nonetheless challenging.

Our second contribution is to develop two approximate posterior inference procedures for our model, to assess their quality, and to demonstrate how to scale approximate inference to an entire astronomical survey. Section 3 and Section 4 present inference procedures based on MCMC and VI, respectively. Neither is a routine application of Bayesian machinery. The MCMC procedure combines annealed importance sampling and slice sampling. The VI procedure breaks with tradition by optimizing with a variant of Newton’s method instead of closed-form coordinate ascent. Section 5 presents experimental results for both inference procedures, applied to synthetic and real astronomical images. We find that MCMC better quantifies uncertainty, but VI is much faster. Section 6 describes scaling VI to the entire Sloan Digital Sky Survey (SDSS) using a supercomputer. To our knowledge, this is the largest-scale reported application of VI by at least one order of magnitude. Section 7 draws conclusions about each inference procedure. We consider not just the runtime and accuracy, but also our experience deriving the algorithms, implementing them, and maintaining code for each inference technique.

**2. Statistical model.** Stars and galaxies radiate photons. An astronomical image records photons—each originating from a particular celestial body or from background atmospheric noise—that pass through a telescope’s lens during an exposure. A single image contains photons from many sources; even a single pixel may capture photons from multiple sources.

Section 2.1 describes our model of light sources. Quantities of interest, such as direction<sup>2</sup>, color, and flux, are random variables. Section 2.2 describes a generative model of astronomical images: the distribution of each pixel’s value—an observed random variable—depends on the latent variables that we aim to infer. Pixel intensities are conditionally independent given these latent random variables. Figure 2 presents our statistical model as a graphical model.

Table 1 lists the model’s structural constants, denoted by capital Roman letters. All are positive integers. None are estimated.

Table 2 lists the model’s random variables, either for a particular light source  $s \in \{1, \dots, S\}$ , or a particular image  $n \in \{1, \dots, N\}$  and a particular pixel  $m \in \{1, \dots, M\}$ . ( $S$ ,  $N$ , and  $M$  appear in Table 1.) All are denoted by lowercase Roman letters. All are scalars except for the color vector  $c_s$  and the direction vector  $u_s$ . Inferring the posterior distribution of the unobserved random variables in Table 2 is the primary problem addressed by this article.

Table 3 lists model parameters. The first eight parameters, which are distinguished by calligraphic font, parameterize the prior. They are estimated by empirical Bayes, as described in Section 2.1.3. The remaining parameters, denoted by lowercase Greek letters, are set by the SDSS pipeline.

2.1. *Light sources.* An astronomical catalog is a table with one row for each light source. The number of light sources,  $S$ , is a constant determined by existing cataloging software (Bertin & Arnouts 1996). Modeling  $S$  as random we defer to future work.

Light sources in our model are either stars or galaxies, as are the vast majority of light sources in the universe. Exceptions include quasars and supernovae. Asteroids, planets, airplanes, and man-made satellites also occasionally appear in astronomical images. For light source  $s = 1, \dots, S$ , the latent random variable

$$(1) \quad a_s \sim \text{Bernoulli}(\mathcal{A})$$

indicates whether it is a star ( $a_s = 1$ ) or a galaxy ( $a_s = 0$ ). Here  $\mathcal{A}$  is the prior probability that a light source is a star. (We discuss how we set  $\mathcal{A}$ , and all other prior parameters, in Section 2.1.3.)

---

<sup>2</sup>A direction is a position on the celestial sphere.

name	brief description	SDSS value
B	number of filter bands	5
E	number of PSF ‘‘eigenimages’’	4
F	number of knots per PSF eigenimage	$51 \times 51$
H	number of rows of pixels per image	2048
I	number of source types (i.e., star, galaxy)	2
J	number of components in the color prior mixture	8
K	number of components in the galaxy mixture model	8
L	number of parameters in a WCS header	16
M	number of pixels per image	$H \times W$
N	number of images	4,690,230
Q	number of knots for the sky background model	$192 \times 256$
S	number of light sources	469,053,874
W	number of columns of pixels per image	1361

Table 1: Structural constants in our model.

name	brief description	units	domain
$a_s$	galaxy / star indicator	unitless	$\{0, 1\}$
$c_s$	colors	magnitude	$\mathbb{R}^{B-1}$
$e_s^{angle}$	angle of galaxy’s major axis	degrees	$[0, 180)$
$e_s^{radius}$	galaxy’s half-light radius	arcseconds	$(0, \infty)$
$e_s^{profile}$	galaxy’s profile mixing weight	unitless	$[0, 1]$
$e_s^{axis}$	galaxy’s minor-major axis ratio	unitless	$(0, 1)$
$r_s$	reference-band flux density	nanomaggies	$[0, \infty)$
$u_s$	direction (longitude, latitude)	degrees	$[0, 360) \times [-90, 90]$
$x_{nm}$	pixel intensity (observed)	photon count	$\{0, 1, 2, \dots\}$

Table 2: Random variables in our model.

name	brief description	domain
$\mathcal{A}$	prior probability a light source is a star	$[0, 1]$
$\mathcal{C}^{weight}$	color prior mixture weights	$\mathbb{R}^{I \times J}$
$\mathcal{C}^{mean}$	color prior mixture component means	$\mathbb{R}^{I \times J \times (B-1)}$
$\mathcal{C}^{cov}$	color prior mixture component covariance matrices	$\mathbb{R}^{I \times J \times (B-1) \times (B-1)}$
$\mathcal{E}^{radius}$	galaxy half-light radius prior parameters	$\mathbb{R}^2$
$\mathcal{E}^{profile}$	galaxy profile prior parameters	$\mathbb{R}^2$
$\mathcal{E}^{axis}$	galaxy axis ratio prior parameters	$\mathbb{R}^2$
$\mathcal{R}$	reference-band flux prior parameters	$\mathbb{R}^{I \times 2}$
$\sigma_n$	sky background model	$\mathbb{R}^Q$
$\psi_n^{calib}$	expected number of photons per nanomaggy	$\mathbb{R}^H$
$\psi_n^{wcs}$	image alignment	$\mathbb{R}^L$
$\psi_n^{weight}$	point spread function loadings	$\mathbb{R}^E$
$\psi_n^{image}$	point spread function principal components	$\mathbb{R}^{E \times F}$
$\beta_n$	filter band	$\{1, 2, \dots, B\}$

Table 3: Parameters in our model.

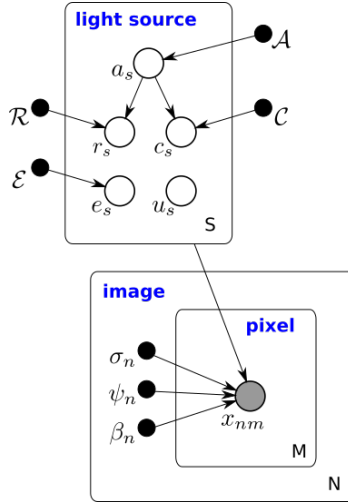


Fig 2: The proposed graphical model. The shaded vertex represents observed random variables. Empty vertices represent latent random variables. Black dots represent constants, set before inference takes place. Edges signify conditional dependencies. Rectangles (“plates”) represent independent replication. Tables 1, 2, and 3 summarize the variables.

The latent random two-vector  $u_s$  denotes the direction of light source  $s$  in the units of the World Coordinate System (Greisen & Calabretta 2002). Figure 9 illustrates this system of coordinates. The first coordinate is longitude and the second coordinate is latitude. Both are measured in degrees.

A priori,  $u_s$  is uniformly distributed over the sphere. Treating light sources as uniformly distributed is a simplification—some regions of the sky are known a priori to have more light sources than others, e.g., the galactic plane. This is known as directional dependence. Additionally, it is a simplification to model light sources as positioned independently of each other; gravity causes some clustering among light sources.

2.1.1. *Flux.* The flux of light source  $s$  is defined as its expected total radiation reaching a unit area of Earth’s surface directly facing  $s$ , per unit of time. We can measure the flux as the portion of this radiation (per square meter per second) that passes through each filter in a standardized filter set. Such a set is called a filter system. These standardized filters are approximately band-pass: each allows most of the energy in a certain band of wavelengths through, while blocking most of the energy outside the band. The physical filters attached to a telescope lens closely match the standardized filters of some filter systems.

The five SDSS filters are named for the wavelengths they are most likely to



let pass: ultraviolet ( $u'$ ), green ( $g'$ ), red ( $r'$ ), near infrared ( $i'$ ), and infrared ( $z'$ ). Figure 8 shows how likely a photon of particular wavelength is to pass through each filter. Fukugita et al. (1996) further describe the SDSS filter system.

We model flux with respect to the  $B = 5$  filters of the SDSS filter system. We designate a particular filter as the “reference” filter, letting the random variable  $r_s$  denote the flux of object  $s$  with respect to that filter. A priori,

$$(2) \quad r_s | (a_s = i) \sim \text{LogNormal}(\mathcal{R}_{i1}, \mathcal{R}_{i2}).$$

Our prior depends on  $a_s$  to reflect that stars tend to have higher flux density than galaxies. The flux density  $r_s$  is measured in nanomaggies (SDSS 2018c, 2017). One nanomaggy is equivalent to  $3.631 \times 10^{-6}$  Jansky. A nanomaggy is a linear unit; we expect to receive twice as many photons from a two-nanomaggy light source as from a one-nanomaggy light source.

The log-normal distribution reflects that flux is non-negative and that stars’ fluxes often differ by orders of magnitude. Empirically, a log-normal distribution fits the SDSS catalog better than any gamma distribution—another common model for non-negative real-valued variables. In future work, we may also explore a power law distribution for galaxy fluxes, as there is some theoretical support for that model.

The flux of light source  $s$  with respect to the remaining  $B - 1$  filters is encoded using colors. The color  $c_{s\beta}$  is defined as the log ratio of fluxes with respect to filters  $\beta$  and  $\beta + 1$ . Here, the filters are ordered by the wavelength bands they let pass. The  $B - 1$  colors for object  $s$  are collectively denoted by  $c_s$ , a random  $(B - 1)$ -vector. We denote the colors as  $u-g$ ,  $g-r$ ,  $r-i$ , and  $i-z$ . The reference-filter flux  $r_s$  and the colors  $c_s$  uniquely specify the flux for light source  $s$  through any filter  $\beta$ , denoted  $\ell_{s\beta}$ .

Our model uses the color parameterization because stars and galaxies have very distinct prior distributions in color space. Indeed, for idealized stars—blackbodies—all  $B - 1$  colors lie on a one-dimensional manifold indexed by surface temperature. On the other hand, though galaxies are composed of stars, theory does not suggest they lie near the same manifold: the stars in a galaxy can have many different surface temperatures, and some of the photons are re-processed to other energies through interactions with dust and gas. Figure 3 demonstrates that stars are much closer to a one-dimensional manifold in color space than galaxies are.

We model the prior distribution on  $c_s$  as a  $D$ -component Gaussian mixture model (GMM):

$$(3) \quad c_s | (a_s = i) \sim \text{GMM}(C_i^{\text{weight}}, C_i^{\text{mean}}, C_i^{\text{cov}}).$$

We discuss how we set  $D$  and the color priors’ hyperparameters in Section 3.

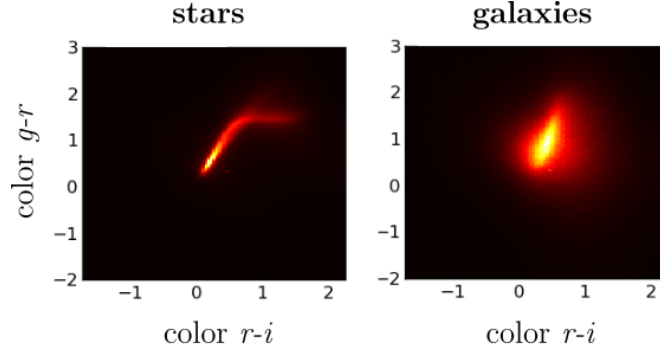


Fig 3: Density plots for two colors,  $g-r$  and  $r-i$ , based on the SDSS catalog.

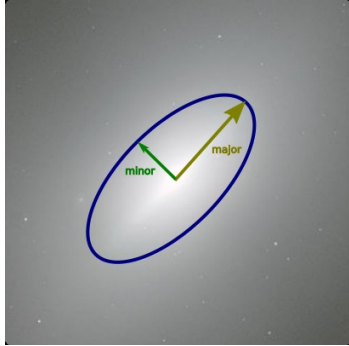


Fig 4: A schematic of the galaxy light kernel. The blue ellipse surrounds half of the light emissions of this galaxy. The length of the major axis is the half-light radius  $e_s^{radius}$ . The angle in degrees of the major axis is  $e_s^{angle} = 45$ . The ratio of the lengths of minor and major axes is  $e_s^{axis} = 1/2$ . Because this galaxy is purely elliptical,  $e_s^{profile} = 0$ .

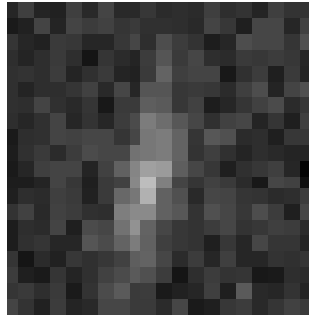
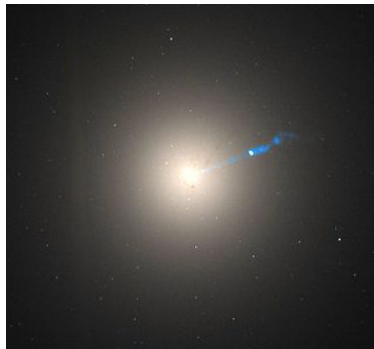
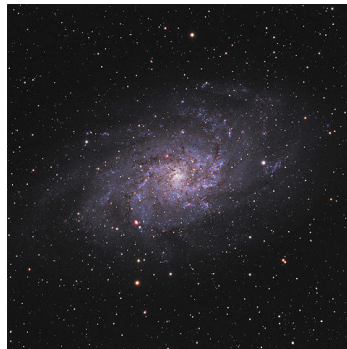


Fig 5: A distant galaxy approximately 20 pixels in height, estimated to have half-light radius  $e_s^{radius} = 0.6$  arcseconds, rotation angle  $e_s^{angle} = 80$  degrees, and minor-major axis ratio  $e_s^{axis} = 0.17$ .



(a) Messier 87, a galaxy that exhibits the de Vaucouleurs profile. Credit: NASA



(b) Triangulum, a galaxy that exhibits the exponential profile. Credit: NASA

Fig 6: Extremal galaxy profiles.

2.1.2. *Spatial extent.* Consider a light source  $s$ , centered at some direction  $u_s$ . Its flux density in filter band  $\beta$ , measured at a possibly different direction  $\mu$ , is given by

$$(4) \quad \varphi_{s\beta}(\mu) := h_s(\mu)\ell_{s\beta}.$$

Here  $h_s$  (a density) models the spatial characteristics of light source  $s$ , quantifying its relative intensity at each direction  $\mu$  specified in sky coordinates (not image-specific ‘‘pixel coordinates’’). We refer to  $h_s$  as the ‘‘light kernel’’ for light source  $s$ .

The distance from Earth to any star other than the Sun exceeds the star’s radius by many orders of magnitude. Therefore, we model stars as point sources. If light source  $s$  is a star (i.e.,  $a_s = 1$ ), then  $h_s$  is simply a delta function: one if  $\mu = u_s$ , zero otherwise.

Modeling the two-dimensional appearance of galaxies as seen from Earth is more involved. If light source  $s$  is a galaxy (i.e.,  $a_s = 0$ ), then  $h_s$  is parameterized by a latent random 4-vector

$$(5) \quad e_s := (e_s^{profile}, e_s^{angle}, e_s^{radius}, e_s^{axis}).$$

We take  $h_s$  to be a convex combination of two extremal profiles, known in astronomy as ‘‘de Vaucouleurs’’ and ‘‘exponential’’ profiles:

$$(6) \quad h_s(\mu) = e_s^{profile}h_{s1}(\mu) + (1 - e_s^{profile})h_{s2}(\mu).$$

The de Vaucouleurs profile is characteristic of elliptical galaxies, whose luminosities vary gradually in space (Figure 6a), whereas the exponential profile

matches spiral galaxies (Figure 6b) (Feigelson & Babu 2012). The profile functions  $h_{s1}(\mu)$  and  $h_{s2}(\mu)$  also account for additional galaxy-specific parameters illustrated in Figure 4. In particular, each profile function is a rotated, scaled mixture of bivariate normal distributions. Rotation angle and scale are galaxy-specific, while the remaining parameters of each mixture are not:

$$(7) \quad h_{si}(\mu) = \sum_{j=1}^J \alpha_{ij} \phi(\mu; u_s, \tau_{ij} \Sigma_s), \quad i = 1 \text{ or } 2.$$

Here the  $\alpha_{ij}$  and the  $\tau_{ij}$  are prespecified constants that characterize the exponential and de Vaucouleurs profiles;  $u_s$  is the center of the galaxy in sky coordinates;  $\Sigma_s$  is a  $2 \times 2$ -covariance matrix shared across the components; and  $\phi$  is the bivariate normal density.

The light kernel  $h_s(\mu)$  is a finite scale mixture of Gaussians: its mixture components have a common mean  $u_s$ ; the isophotes (level sets of  $h_s(\mu)$ ) are concentric ellipses. Although this model prevents us from fitting individual “arms,” like those of the galaxy in Figure 6b, most galaxies are not sufficiently resolved to see such substructures. Figure 5 shows a more typical galaxy image.

The spatial covariance matrix  $\Sigma_s$  is parameterized by a rotation angle  $e_s^{angle}$ , an eccentricity (minor-major axis ratio)  $e_s^{axis}$ , and an overall size scale  $e_s^{radius}$ :

$$(8) \quad \Sigma_s := R_s^\top \begin{bmatrix} [e_s^{radius}]^2 & 0 \\ 0 & [e_s^{axis}]^2 [e_s^{radius}]^2 \end{bmatrix} R_s,$$

where the rotation matrix is given by

$$(9) \quad R_s := \begin{bmatrix} \cos e_s^{angle} & -\sin e_s^{angle} \\ \sin e_s^{angle} & \cos e_s^{angle} \end{bmatrix}.$$

The scale  $e_s^{radius}$  is specified in terms of half-light radius—the radius of the disc that contains half of the galaxy’s light emissions before applying the eccentricity  $e_s^{angle}$ .

All four entries of  $e_s$  are random. The mixing weight prior is given by

$$(10) \quad e_s^{profile} \sim \text{Beta}(\mathcal{E}_1^{profile}, \mathcal{E}_2^{profile}).$$

Every angle is equally likely, and galaxies are symmetric, so

$$(11) \quad e_s^{angle} \sim \text{Uniform}([0, 180]).$$

We found that the following half-light-radius distribution fit well empirically:

$$(12) \quad e_s^{radius} \sim \text{LogNormal}(\mathcal{E}_1^{radius}, \mathcal{E}_2^{radius}).$$

The “fatter” tail of a log-normal distribution fits better than a gamma distribution, for example. A priori, the minor-major axis ratio is beta distributed:

$$(13) \quad e_s^{axis} \sim \text{Beta}(\mathcal{E}_1^{axis}, \mathcal{E}_2^{axis}).$$

2.1.3. *Setting the priors’ parameters.* Our light source prior has 1099 hyperparameters. All but ten are for the GMM color prior. Empirical Bayes is an appealing way to fit this prior because the number of parameters is small relative to the number of light sources (hundreds of millions for SDSS).

Unfortunately, re-fitting the prior parameters iteratively during inference—a common way of performing empirical Bayes—is difficult in a distributed setting: fitting the global prior parameters during inference couples together numerical optimization for disparate regions of sky. Instead, we fit the prior parameters based on existing SDSS catalogs through maximum likelihood estimation. Because these prior parameters are fit to a catalog based on the same data we subsequently analyze, this is an empirical Bayes procedure.

If the depth of our catalog were much greater than existing SDSS catalogs, we might refit these prior parameters periodically while performing inference. Refitting in this way could be interpreted as a block coordinate ascent scheme. However, in our work to date, the depth of our catalog is limited by the peak-finding preprocessing routine, just as in SDSS. Therefore, for simplicity, we hold these prior parameters fixed during inference.

Fitting the color prior warrants some additional discussion. First, maximum-likelihood estimation for a GMM is nonconvex, so the optimization path may matter: we use the `GaussianMixture.jl` software (van Leeuwen 2018). Second, we set the number of GMM components  $D$  based on computational considerations. In principle,  $D$  could be set with a statistical model-selection criterion. In practice, we set  $D = 8$  without any apparent accuracy reduction for the point estimates, which is the primary way we assess our model in Section 5. Because we have so much data (millions of light sources), there is no risk of overfitting with  $D = 8$ : held-out log-likelihood improves as  $D$  increases up to  $D = 256$ , the largest setting our hardware allowed us to test. There is also little risk that  $D = 8$  underfits: setting  $D = 16$  does not substantively change our estimates.

Empirical Bayes seems broadly applicable to sky-survey data; the number of light sources in typical surveys is large relative to the number of hyperparameters. But the details of our procedure (e.g., how to set  $D$ , or whether

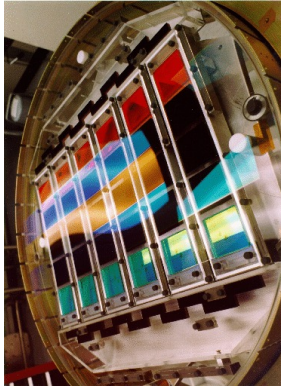


Fig 7: The SDSS camera. Its CCDs—each  $2048 \times 2048$  pixels—are arranged in six columns and five rows. A different filter covers each row. Credit: [SDSS \(2018a\)](#).

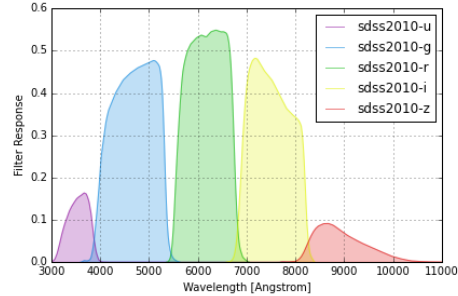


Fig 8: SDSS filter curves. Filter response is the probability that a photon of a particular wavelength will pass through the filter. Credit: [Doi et al. \(2010\)](#).

to update the hyperparameters iteratively during inference) may need to be tailored based on the research goals. If so, our fitted priors may be considered “interim” priors.

**2.2. Images.** Astronomical images are taken through telescopes. Photons that enter the telescope reach a camera at its base that records the pixel each photon hits, thus contributing an electron. The SDSS camera (Figure 7) consists of 30 charge-coupled devices (CCDs) arranged in a grid of six columns and five rows. Each row is covered by a different filter—transparent colored glass that limits which photons can pass through and potentially be recorded. Each of the five filters selects, stochastically, for photons of different wavelengths (Figure 8). Multiple images of the same region of the sky with different filters reveal the colors of stars and galaxies.

The SDSS telescope collects images by drift scanning, an imaging regime where the camera reads the CCDs continuously as the photons arrive. Each night the telescope images a contiguous “arc” of sky (Figure 9).

Each arc is divided into multiple image files. SDSS contains  $N = 4,690,230$  of these images, each taken through one of the 30 CCDs. For  $n = 1, \dots, N$ , the constant  $\beta_n$  denotes the filter color for image  $n$ .

Each image is a grid of  $M = 2048 \times 1361$  pixels. The random variable  $x_{nm}$  denotes the count of photons that, during the exposure for image  $n$ , entered the telescope, passed through the filter, and were recorded by pixel  $m$ .

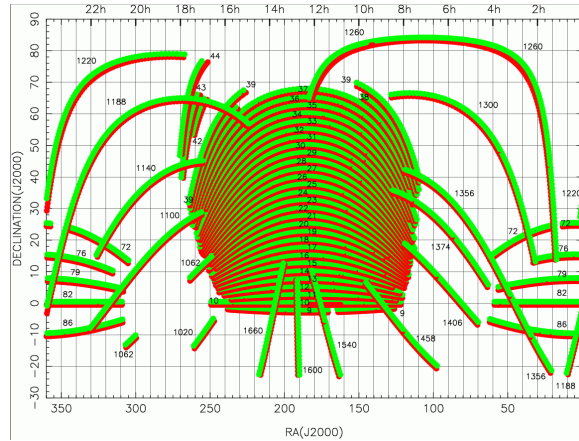


Fig 9: SDSS sky coverage map. Each monochrome arc represents the sky photographed during a particular night. Axes’ units are degrees of right ascension (longitude) and declination (latitude). Credit: [SDSS \(2018d\)](#).

2.2.1. *Skyglow.* The night sky is not completely dark, even in directions without resolvable light sources. This is due to both artificial light production (e.g., light pollution from cities) and natural phenomena. The background flux is called “skyglow.” Sources of natural skyglow include sunlight reflected off dust particles in the solar system, nebulosity (i.e., glowing gas—a constituent of the interstellar medium), extragalactic background light from distant unresolved galaxies, night airglow from molecules in Earth’s atmosphere, and scattered starlight and moonlight. The flux from skyglow (“sky intensity”) varies by the time of the exposure, due to changing atmospheric conditions. It also varies with direction; for example, sky intensity is typically greater near the galactic plane. We model skyglow as a spatial Poisson process whose rate varies gradually by pixel, independent of stars and galaxies. For the vast majority of pixels, the skyglow is the only source of photons.

Sky intensity is estimated during preprocessing by pre-existing software ([Bertin & Arnouts 1996](#)) and fixed during inference. This software fits a smooth parametric model to the intensities of the pixels that it determines are not near any light source. The sky intensity could, in principle, be fit within our inference procedure; we defer this idea to future work.

The sky intensity for image  $n$  is stored as a grid of  $Q$  intensities in the matrix  $\sigma_n$ . Typically  $Q \ll M$  because the sky intensity varies slowly. To form the sky intensity for a particular pixel,  $\sigma_n$  is interpolated linearly. We denote the sky intensity for a particular pixel by  $\sigma_n(m)$ .

2.2.2. *Point-spread functions.* Astronomical images are blurred by a combination of small-angle scattering in Earth’s atmosphere, the diffraction limit of the telescope, optical distortions in the camera, and charge diffusion within the silicon of the CCD detectors. Together these effects are represented by the “point-spread function” (PSF) of a given image. Stars are essentially point sources, but the PSF represents how their photons are spread over dozens of adjacent pixels.

The PSF is set during preprocessing by pre-existing software (Lupton et al. 2001). This software fits the PSF based on several stars with extremely high flux in each image whose characteristics are well established by previous studies using different instrumentation (e.g., spectrographs). As with sky intensity, we could fit the PSF jointly with light sources through our approximate inference procedure, but we do not pursue this idea here.

The PSF is specified through several image-specific parameters that are bundled together in  $\psi_n$ . The vector  $\psi_n^{calib}$  gives the expected number of photons per nanomaggy for each column of image  $n$ . The vector  $\psi_n^{wcs}$  specifies a mapping from sky direction to pixel coordinates. This mapping is linear—an approximation that holds up well locally. The rows of the matrix  $\psi_n^{image}$  give the top principal components from an eigendecomposition of the PSF as rendered on a grid centered at a light source. The vector  $\psi_n^{weight}$  gives the loading of the PSF at any point in the image. It has smooth spatial variation.

Consider a one-nanomaggy star having direction  $\mu$ . We denote its expected contribution of photons to the  $m$ th pixel of image  $n$  as  $g_{nm}(\mu)$ ; this is derived as needed from the explicitly represented quantities discussed above.

2.2.3. *The likelihood.* Let  $z_s := (a_s, r_s, c_s, e_s, u_s)$  denote the latent random variables for light source  $s$ . Let  $z := \{z_s\}_{s=1}^S$  denote all the latent random variables. Then, for the number of photons received by pixel  $m$  of image  $n$ , we take the likelihood to be

$$(14) \quad x_{nm}|z \sim \text{Poisson}(\lambda_{nm}).$$

The dependence of  $\lambda_{nm}$  on  $z$  is not notated here. We model  $x_{nm}$  as observed, though the reality is somewhat more complicated (SDSS 2018b): at the end of an exposure, the CCD readout process transfers the electrons to a small capacitor, converting the (discrete) charge to an (analog/continuous) voltage (at the microvolt level) that is amplified and forms the output of the CCD chip. The net voltage is measured and digitized by an analog-to-digital converter (ADC). The conversion is characterized by a conversion gain. The ADC output is an integer called a digital number (DN). The conversion gain is specified in terms of electrons per DN.<sup>3</sup>

<sup>3</sup>We thank an anonymous reviewer for a precise explanation, which we paraphrase here.



Because of these complexities, it is not clear whether a Poisson distribution is more suitable here than a Gaussian distribution with its mean equal to its variance. We make no claims about the superiority of one or the other. In the SDSS, the sky background is typically at least 500 electrons per pixel, so it seems unlikely that the choice of a Gaussian (with its mean equal to its variance) or a Poisson distribution would matter. Furthermore, neither likelihood simplifies the subsequent inferential calculations.

In Equation 14, the rate parameter  $\lambda_{nm}$  is unique to pixel  $m$  in image  $n$ . It is a deterministic function of the catalog (which includes random quantities) given by

$$(15) \quad \lambda_{nm} := \sigma_n(m) + \sum_{s=1}^S \ell_{s\beta_n} \int g_{nm}(\mu) h_s(\mu) d\mu.$$

The summation over light sources reflects the assumption that light sources do not occlude one another, or the skyglow. The integral is over all sky locations. In practice, it can be restricted to pixels near pixel  $m$ —distant light sources contribute a negligible number of photons. Our implementation bases this distance measurement on conservative estimates of light sources’ extents from SExtractor (Bertin & Arnouts 1996). As shorthand, we denote the integral as

$$(16) \quad f_{nms} := \int g_{nm}(\mu) h_s(\mu) d\mu.$$

If light source  $s$  is a star, then it is straightforward to express  $f_{nms}$  analytically:

$$(17) \quad f_{nms} = g_{nm}(u_s).$$

If light source  $s$  is a galaxy, the same integral is more complex because galaxies have spatial extent. Our approach is to approximate  $\psi_n$  with a mixture of bivariate normal densities. Because Gaussian-Gaussian convolution is analytic, we get an analytic approximation to  $f_{nms}$ .

Our primary use for the model is computing the posterior distribution of its unobserved random variables conditional on a particular collection of astronomical images. We denote the posterior by  $p(z|x)$ , where  $x := \{x_{nm}\}_{n=1, m=1}^{N, M}$  represents all the pixel intensities. Exact posterior inference is computationally intractable for the proposed model, as it is for most non-trivial probabilistic models. The next two sections consider two approaches to approximate posterior inference: Markov chain Monte Carlo (MCMC) and variational inference (VI).

**3. Markov chain Monte Carlo.** Markov chain Monte Carlo (MCMC) is a common approach for approximating posterior distributions in computationally challenging Bayesian models. MCMC draws samples from a stochastic process on the parameter space whose stationary distribution is the posterior distribution of interest. The stochastic process is specified by a transition kernel, denoted  $\mathcal{T}$ . The empirical distribution of these samples approximates the posterior distribution. Statistics of this empirical distribution, such as its mean and its quantiles, approximate the same statistics of the posterior distribution.

Our problem presents two unique challenges for MCMC. First, the state space is extremely high-dimensional—there are multiple random variables for each of millions of light sources. We cannot consider transition kernels that require hand-tuning of dimension-specific parameters, such as step size, proposal variance, or temperature schedule. Second, the state space is trans-dimensional. Galaxies have more parameters than stars, and light source types (star/galaxy) are themselves random.

We propose a multi-level sampling procedure. In an outer loop based on (block) Gibbs sampling (Bishop 2006), light sources are typically treated sequentially. Each light source’s latent variables are sampled with any overlapping light sources’ latent variables, denoted  $z_{-s}$ , held fixed. Formally, in Gibbs iteration  $k = 1, \dots, K$ , we draw

$$(18) \quad z_s^{(k)} \sim p(z_s | x, z_{-s})$$

for light sources  $s = 1, \dots, S$  in sequence. To speed up convergence, we initialize  $z_1^{(0)}, \dots, z_S^{(0)}$  with approximately correct values determined by a preprocessing routine. This is a valid procedure for sampling from the posterior.

The inner loop, based on annealed importance sampling (AIS) (Neal 2001), is our procedure for drawing from  $p(z_s | x, z_{-s})$ .

3.1. *Estimating the marginal likelihood.* We simulate posterior samples by first separately measuring how well the star and galaxy models explain the observation  $x$ . First, we use AIS to estimate

$$(19) \quad p(a_s = 1 | x, z_{-s}).$$

Recall  $a_s$  is the Bernoulli random variable that indexes the source type (star/galaxy), and thus the dimension of our state space. AIS allows us to avoid using a trans-dimensional sampler like reversible-jump MCMC (Green 1995), a technique that requires constructing a potentially complex trans-dimensional proposal function (Fan & Sisson 2011).

AIS is an iterative procedure to estimate the normalizing constant of an unnormalized probability density  $\pi$ . In order to estimate distribution in Equation 19, we estimate

$$(20) \quad \pi(z_s) := p(x|z_s, a_s, z_{-s})p(z_s|a_s, z_{-s})$$

for both both source types,  $a_s = 0$  and  $a_s = 1$ . The normalizing constant of  $\pi$  is  $p(x|a_s, z_{-s})$ . Given an estimate of  $p(x|a_s, z_{-s})$  (for both settings of  $a_s$ ) and a prior over  $a_s$ , we can construct an estimate of  $p(a_s|x, z_{-s})$  using Bayes rule. Given a sample from  $p(a_s|x, z_{-s})$ , we can conditionally simulate an approximate posterior sample of the source type-specific parameters,  $p(z_s|a_s, z_{-s}, x)$ , using MCMC transitions.

In addition to the target  $\pi$ , AIS takes as input a sequence of  $T$  distributions  $\pi_0, \pi_1, \dots, \pi_T$  that approach the target. The statistical efficiency of AIS depends on the similarity of intermediate distributions  $\pi_{t-1}(z_s)/\pi_t(z_s)$ . We set  $\pi_0(z_s) := p(z_s|a_s = 1, z_{-s})$ —a normalized density. For  $t = 1, \dots, T$ , we set

$$(21) \quad \pi_t(z_s) = \pi_0(z_s)^{1-\gamma_t} \pi(z_s)^{\gamma_t}$$

for a sequence of temperatures  $0 = \gamma_0 < \gamma_1 < \dots < \gamma_T = 1$ . These (unnormalized) distributions interpolate between the prior and the posterior.

For  $t = 1, \dots, T$ , let  $\mathcal{T}_t$  be a Markov chain transition that leaves (the normalized version of)  $\pi_t$  invariant. To implement each transition kernel,  $\mathcal{T}_t$ , we use slice sampling, a Markov chain Monte Carlo method that requires no tuning and automatically adapts to the local scale for each variable (Neal 2003). We iterate over each variable in  $z_s$ , forming a slice-sampling-within-Gibbs transition kernel.

We begin by sampling  $z_s^{(0)} \sim \pi_0$ . Then, for  $t = 1, \dots, T$ , we draw

$$(22) \quad z_s^{(t)} | z_s^{(t-1)} \sim \mathcal{T}_t(z_s^{(t-1)}, z_s^{(t)}).$$

After  $T$  iterations,  $z_s^{(T)}$  is approximately distributed according to (the normalized version of)  $\pi_T = \pi$ , and

$$(23) \quad \mathcal{Z}_s := \exp \sum_{t=1}^T \log \frac{\pi_t(z_s^{(t-1)})}{\pi_{t-1}(z_s^{(t-1)})}$$

is a consistent estimator of  $p(x|a_s = 1, z_{-s})$  (Neal 2001). AIS can be viewed as importance sampling over an augmented state-space where the expanded dimensions begin with the prior distribution and gradually anneal to the targeted posterior according to  $T$  temperatures. Thus, the ratio of these weights is a consistent estimator of the marginal likelihood.

Estimating the marginal likelihood (also referred to as the model evidence) is a rich area of methodological development. [Skilling \(2004\)](#) presents another popular approach for computing marginal likelihood estimates, known as nested sampling. However, [Friel & Wyse \(2012\)](#) show cases where nested sampling is less efficient statistically and computationally than AIS, motivating our use of AIS in this work.

**3.2. Sampling with AIS.** The final step of our AIS procedure draws samples from  $p(z_s|x, z_{-s})$ . For each source type (star/galaxy), we run  $N'$  independent repetitions of our AIS procedure. We use the resulting samples as independent starting positions for  $N'$  Markov chains. We run these  $N'$  chains for  $B'$  more steps, monitoring convergence and mixing criteria ([Gelman & Rubin 1992](#)). This process yields  $N'$  estimates of the marginal likelihood, and  $N' \times B'$  (correlated) samples drawn from the Markov chain.

The summarize, the overall AIS-MCMC sampling procedure corresponding to Equation 18 is as follows:

- For each source type  $a_s = a \in \{0, 1\}$  (e.g., star or galaxy)
  - Run  $N'$  *independent* marginal likelihood estimators, each with  $T$  annealing steps. This results in  $N'$  independent estimates of  $\log p(x|a_s = a, z_{-s})$  and  $N'$  approximate posterior samples from  $p(z_s|a_s = a, x, z_{-s})$ .
  - For each  $N'$  approximate posterior samples, run an MCMC chain of length  $B'$  (e.g., using slice-sampling-within-Gibbs transitions)
- Use the  $\log p(x|a_s = 0, z_{-s})$  and  $\log p(x|a_s = 1, z_{-s})$  estimates to approximate  $p(a_s = a|x, z_{-s})$
- Use the  $N' \times B'$  samples to approximate  $p(z_s|a_s = a)$  for both source types  $a \in \{0, 1\}$ .
- Use the estimate of  $p(a_s = a|x, z_{-s})$  to sample a source type  $a_s^{(k)}$ . Simulate  $z_s^{(k)} \sim p(z_s|x, z_{-s}, a_s)$  by randomly choosing one of the  $N'$  posterior samples for the sampled source-type  $a_s^{(k)}$  to generate samples according to Equation 18.

The AIS-MCMC procedure described above requires us to choose a number of samples and iterations. For the experiments we describe in Section 5, we use  $T = 200$  annealing steps and  $N' = 25$  independent samples of the marginal likelihood. For each  $N'$  sample, we run an additional slice-sampling MCMC chain for  $B' = 25$  iterations, producing a total of of  $N' \times B' = 625$  correlated posterior samples of  $z_s$ .

**4. Variational inference.** Variational inference (VI) chooses an approximation to the posterior distribution  $p(z|x)$  from a class of candidate distributions via numerical optimization. The candidate approximating distributions  $q_\theta(z)$ , called “variational distributions”, are parameterized by a real-valued vector  $\theta$ . Through numerical optimization, VI minimizes (with respect to  $\theta$ ) the KL divergence between  $q_\theta(z)$  and  $p(z|x)$ .

For an introduction to VI, we recommend [Blei et al. \(2017\)](#) to statisticians, [MacKay \(1995\)](#) to physicists, and [Šmídl & Quinn \(2006\)](#) to readers with a background in signal processing.

4.1. *The variational distributions.* We restrict the variational distributions to a class that makes KL minimization tractable. Our variational distributions all factorize:

$$(24) \quad q_\theta(z) = \prod_{s=1}^S q(a_s)q(u_s)q(e_s)q(r_s|a_s)q(c_s|a_s).$$

We have suppressed the subscript  $\theta$  in the variational factors. This is not quite mean-field variational inference ([Blei et al. 2017](#)), where the variational distribution factorizes across all random variables, because some factors are conditional on  $a_s$  (i.e., whether a light source is a star or a galaxy). The next equations show the constituents of  $\theta$ . We use “acute” and “hat” accents to denote variational parameters. For  $s = 1, \dots, S$  and  $i \in \{0, 1\}$  we take

$$(25) \quad q(a_s) \sim \text{Bernoulli}(\acute{a}_s),$$

$$(26) \quad q(r_s|a_s = i) \sim \text{LogNormal}(\acute{r}_{si}, \hat{r}_{si}),$$

$$(27) \quad q(c_s|a_s = i) \sim \text{MvNormal}(\acute{c}_{si}, I\hat{c}_{si}),$$

$$(28) \quad q(u_s) \sim \text{PointMass}(\acute{u}_s),$$

$$(29) \quad q(e_s) \sim \text{PointMass}(\acute{e}_s).$$

Here  $\acute{e}_s := (\acute{e}_s^{\text{angle}}, \acute{e}_s^{\text{radius}}, \acute{e}_s^{\text{profile}}, \acute{e}_s^{\text{axis}})$ .

Approximating the posterior for  $u_s$  and  $e_s$  with a point mass is a strong assumption. It is analogous to performing maximum a posteriori (MAP) inference for these parameters. We do so only because of computational considerations: it lets us write the objective function as an analytic expression. Analytic expressions can be optimized efficiently by deterministic numerical optimization routines, which in turn can converge much faster than stochastic optimization ([Bubeck 2015](#)). Ongoing research aims to expand the class of models and variational distributions that can be optimized with deterministic VI, though limitations persist ([Frayssé & Rodet 2014](#), [Zheng et al. 2015](#), [Giordano et al. 2015](#)).

4.2. *The variational lower bound.* Because  $p(x)$  is constant with respect to  $\theta$ , minimizing  $D_{\text{KL}}(q_\theta(z), p(z|x))$  is equivalent to maximizing

$$(30) \quad \mathcal{L}(\theta) := \mathbb{E}_{q_\theta} [\log p(x|z)] - D_{\text{KL}}(q_\theta(z), p(z)).$$

Maximization of  $\mathcal{L}(\theta)$  is the standard approach; see [Blei et al. \(2017\)](#) for discussion.

The first term of  $\mathcal{L}(\theta)$  is the expected log likelihood of the data. It is

$$(31) \quad \mathbb{E}_q [\log p(x|z)] = \sum_{n=1}^N \sum_{m=1}^M \{-\mathbb{E}_q [\lambda_{nm}] + x_{nm} \mathbb{E}_q [\log \lambda_{nm}] - \log(x_{nm}!)\}.$$

4.2.1. *Expectation of the rate parameter.* The first expectation is

$$(32) \quad \mathbb{E}_q [\lambda_{nm}] = \sigma_{nm} + \sum_{s=1}^S \mathbb{E}_q [\ell_{s\beta_n} f_{nms}].$$

We can factorize the right-hand expectation based on the factorization of the variational distribution, upon conditioning on  $a_s$ :

$$(33) \quad \begin{aligned} \mathbb{E}_q [\ell_{s\beta_n} f_{nms}] &= (1 - \acute{a}_s) \mathbb{E}_q [\ell_{s\beta_n} | a_s = 0] \mathbb{E}_q [f_{nms} | a_s = 0] \\ &\quad + \acute{a}_s \mathbb{E}_q [\ell_{s\beta_n} | a_s = 1] \mathbb{E}_q [f_{nms} | a_s = 1]. \end{aligned}$$

The integral  $\mathbb{E}_q [\ell_{s\beta} | a_s]$  is tractable because flux  $r_s$  and each entry of  $c_s$  (the colors) are independent in the variational distribution given  $a_s$ . The integral  $\mathbb{E}_q [f_{nms} | a_s]$  is tractable because  $u_s$  is a point mass in the variational distribution.

4.2.2. *Expectation of the log rate parameter.* We approximate the expected logarithm of  $\lambda_{nm}$  using the delta method for moments ([Bickel & Doksum 2015](#)). We replace the integrand with a second-order Taylor expansion around its mean:

$$(34) \quad \begin{aligned} \log(\lambda_{nm}) &\approx \log \mathbb{E}_q [\lambda_{nm}] + \frac{1}{\mathbb{E}_q [\lambda_{nm}]} (\lambda_{nm} - \mathbb{E}_q [\lambda_{nm}]) \\ &\quad - \frac{1}{2\mathbb{E}_q [\lambda_{nm}]^2} (\lambda_{nm} - \mathbb{E}_q [\lambda_{nm}])^2. \end{aligned}$$

Then, taking expectations,

$$(35) \quad \mathbb{E}_q [\log(\lambda_{nm})] \approx \log \mathbb{E}_q [\lambda_{nm}] - \frac{\mathbb{V}_q [\lambda_{nm}]}{2\mathbb{E}_q [\lambda_{nm}]^2},$$

where  $\mathbb{V}_q$  denotes variance with respect to the variational distribution  $q$ . That term may be further expanded:

$$(36) \quad \mathbb{V}_q[\lambda_{nm}] = \sum_{s=1}^S \mathbb{V}_q[\ell_{s\beta_n} f_{nms}]$$

$$(37) \quad = \sum_{s=1}^S \mathbb{E}_q[\ell_{s\beta_n}^2 f_{nms}^2] - (\mathbb{E}_q[\ell_{s\beta_n} f_{nms}])^2.$$

The second expectation on the right-hand side is given in Equation 33. The first is

$$(38) \quad \begin{aligned} \mathbb{E}_q[\ell_{s\beta_n}^2 f_{nms}^2] &= (1 - \acute{a}_s) \mathbb{E}_q[\ell_{s\beta_n}^2 | a_s = 0] \mathbb{E}_q[f_{nms}^2 | a_s = 0] \\ &\quad + \acute{a}_s \mathbb{E}_q[\ell_{s\beta_n}^2 | a_s = 1] \mathbb{E}_q[f_{nms}^2 | a_s = 1]. \end{aligned}$$

4.2.3. *KL divergence.* Because of the factorization of the variational distribution, the KL term in Equation 30 separates across sources:

$$(39) \quad D_{\text{KL}}(q(z), p(z)) = \sum_{s=1}^S D_{\text{KL}}(q(z_s), p(z_s)).$$

It separates further within each source:

$$(40) \quad \begin{aligned} D_{\text{KL}}(q(z_s), p(z_s)) &= D_{\text{KL}}(q(a_s), p(a_s)) \\ &\quad + D_{\text{KL}}(q(u_s), p(u_s)) + D_{\text{KL}}(q(e_s), p(e_s)) \\ &\quad + \sum_{i=0}^1 q(a_s = i) \left[ D_{\text{KL}}(q(r_s | a_s = i), p(r_s | a_s = i)) \right. \\ &\quad \left. + D_{\text{KL}}(q(c_s | a_s = i), p(c_s | a_s = i)) \right]. \end{aligned}$$

Except for the last, these KL divergences are between common exponential family distributions. We give formulas for them in [Supplement A](#).

The last KL divergence is more complicated because the prior on  $c_s$  is a Gaussian mixture model. We take the eighth approach from [Hershey & Olsen \(2007\)](#) to identify an upper bound on this KL divergence:

$$(41) \quad \begin{aligned} D_{\text{KL}}(q(c_s | a_s = i), p(c_s | a_s = i)) \\ \leq D_{\text{KL}}(\xi_i, C_i^{\text{weights}}) + \sum_{j=1}^J \xi_{ij} D_{\text{KL}}(q(c_s | a_s = i), C_{ij}). \end{aligned}$$

Here  $C_i^{\text{weights}}$  is the categorical distribution over the color prior's mixture components,  $C_{ij}$  is the color prior's  $j$ th mixture component, and  $\xi_i \in [0, 1]^J$

is a vector of free parameters. To make the bound as tight as possible, we optimize the  $\xi_i$  along with the variational lower bound. The optimal  $\xi_i$  can also be expressed analytically in terms of  $\mathcal{C}_i$ :

$$(42) \quad \xi_{ij}^* \propto \mathcal{C}_{ij}^{weights} \exp\{-D_{\text{KL}}(q(c_s|a_s = i), \mathcal{C}_{ij})\}.$$

4.3. *Numerical optimization.* Traditionally, variational lower bounds are maximized through coordinate ascent: each update sets a variational parameter to its optimal value with the others held fixed (Bishop 2006, Murphy 2012). This approach is simple to implement because gradients and Hessians do not need to be explicitly computed. Each update increases the variational lower bound. The algorithm converges to a local optimum even for nonconvex objective functions. However, coordinate ascent can take many iterations to converge when the Hessian of the objective function is not diagonal. Additionally, for many models, including ours, optimal coordinate ascent updates cannot be expressed analytically.

Instead, we propose an optimization procedure based on *block* coordinate ascent. Each light source corresponds to a block of 44 parameters: the 37 variational parameters in Equations 25–29 and the 7-dimensional parameter  $\xi$ . We optimize each block by calling a subsolver, explained in the next paragraph. Because most pairs of light sources do not overlap, the Hessian has low fill off the block diagonal. Block coordinate ascent converges quickly in this setting: for light sources that do not overlap with any other light source, just one update step, based on one call to a subsolver, is required to reach a local maximum. For groups of light sources that overlap with each other, a few passes over each light source suffice in practice. Light sources may be optimized in a round-robin order or at random.

As a subsolver to optimize one block of parameters with all others fixed, we use Newton’s method with a trust-region constraint that restricts each step to a Euclidean ball centered at the previous iterate (Nocedal 2006). The trust-region constraint ensures that we find a local maximum even though the variational objective is nonconvex. The method consistently converges in tens of iterations, whereas first-order methods take thousands. BFGS (Nocedal 2006) also on occasion required thousands of iterations per call. Newton iterations are more expensive computationally than the iterations of first-order methods because the former require computing a dense Hessian along with each gradient. For our objective function, computing both a Hessian and a gradient takes  $3\times$  longer than computing a gradient alone. In the end, we gain at least an order of magnitude speedup by using Newton’s method rather than a gradient-only method because the former requires many fewer iterations.



4.4. *Distributed optimization.* Modern compute clusters and supercomputers contain many individual *compute nodes* that execute instructions in parallel. Additionally, each compute node runs many *threads* in parallel—at least one per CPU core. Communication among compute nodes is orders of magnitude slower than communication among threads on the same node.

Block coordinate ascent (the outer loop of our optimization procedure) is a serial algorithm: if multiple blocks of parameters are updated simultaneously based on the current iterate, the objective value may decrease, and the algorithm may diverge. By taking advantage of the structure of our problem, however, we parallelize block coordinate ascent across both compute nodes and CPU cores. Equation 31 is a sum over pixels and Equation 39 is a sum over light sources. Therefore, our objective function may be expressed as a sum whose terms each depend on the parameters for at most one light source from any particular collection of non-overlapping light sources. Thus, for any collection of non-overlapping light sources, maximizing over each light source’s parameters serially is equivalent to maximizing over all these light sources’ parameters in parallel.

Each compute node is tasked with optimizing all the light sources in a region of the sky. Because these light sources are physically near each other, they appear in many of the same images; we only need to load these images once for to infer parameters for all these light sources. Each node implements a locking mechanism that prevents its threads from optimizing overlapping light sources simultaneously. Because within-node communication is fast, there is almost no overhead from this type of locking mechanism.

Communication between nodes is relatively slow. We avoid using an inter-node locking mechanism by assigning each node to optimize different regions of the sky. Because the boundaries of these regions are small relative to the interior, we find an iterate near a stationary point with this approach. A second pass with shifted boundaries ensures that even light sources near a boundary during the first pass are fully optimized.

**5. Experimental results.** Our experiments aim to assess 1) whether the proposed model is a viable alternative to current software pipelines; 2) how MCMC and VI compare, statistically and computationally; and 3) how well our procedures quantify uncertainty.

We base our experiments both on synthetic images drawn from our model (Section 5.1) and images from the Sloan Digital Sky Survey (Section 5.2). For both datasets, we run both the MCMC procedure from Section 3 (henceforth, MCMC) and the variational inference procedure from Section 4 (henceforth, VI), and compare their posterior approximations.<sup>4</sup>

We assess the accuracy of point estimates (e.g., posterior means/modes) and uncertainties (e.g., posterior variances), as well as star/galaxy classification accuracy. Our accuracy measures are averaged over a population of light sources. While no single metric of quality suffices for all downstream uses of catalogs, good performance on the metrics we report is necessary (though perhaps not always sufficient) for good performance on most downstream tasks.

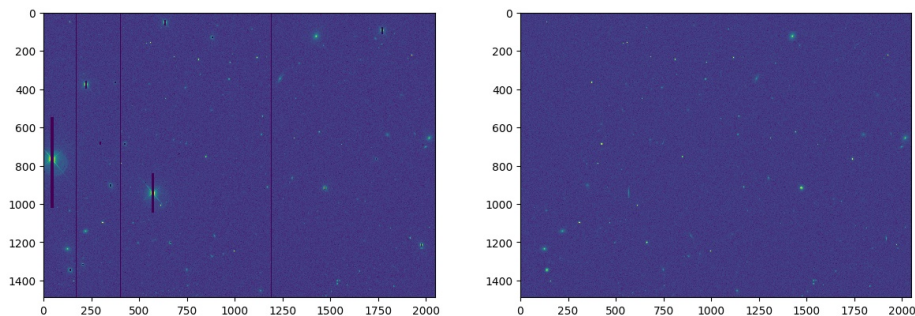
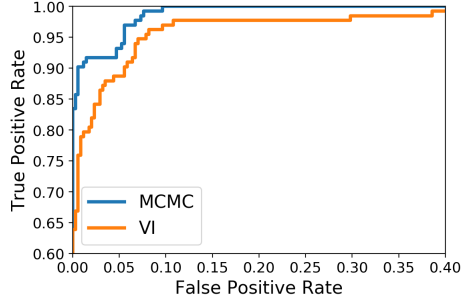


Fig 10: *Left:* An image from SDSS containing approximately 1000 detectable light sources. Pixels in error are “masked” (black strips). *Right:* A synthetic image for the same region, generated from our model by conditioning on an SDSS catalog for that region. (Several of the light sources with extremely high flux are excluded—the CCDs cannot record such high flux.)

5.1. *Synthetic images.* Synthetic images let us compare inference methods without model misspecification. On synthetic images, “ground truth” for the latent random variables is known. Synthetic images also let us validate our model by visually checking their similarity to real images. To generate realistic synthetic images, we take the non-inferred parameter values from real

<sup>4</sup>Open-source software implementing our inference procedures is available from <https://github.com/jeff-regier/Celeste.jl>. Jupyter notebooks demonstrating how to replicate all reported results are stored in the `experiments` directory.



	MCMC	VI	VI-MCMC
direction	0.111	0.121	<b>0.010</b> ( $\pm 0.003$ )
flux	0.093	0.118	<b>0.025</b> ( $\pm 0.006$ )
color u-g	0.327	0.333	0.006 ( $\pm 0.008$ )
color g-r	0.128	0.126	-0.002 ( $\pm 0.004$ )
color r-i	0.112	0.110	-0.002 ( $\pm 0.005$ )
color i-z	0.154	0.144	-0.010 ( $\pm 0.005$ )
galaxy profile	0.158	0.229	<b>0.072</b> ( $\pm 0.011$ )
galaxy axis	0.074	0.106	<b>0.032</b> ( $\pm 0.006$ )
galaxy radius	0.450	0.688	<b>0.237</b> ( $\pm 0.043$ )
galaxy angle	9.642	8.943	-0.699 ( $\pm 0.437$ )

Fig 11: ROC curve for star/galaxy classification on synthetic data.

Table 4: Left columns: Mean absolute error on synthetic data. **Lower is better.** Right column: Pairwise error differences (and standard error). Statistically significant differences appear in bold font.

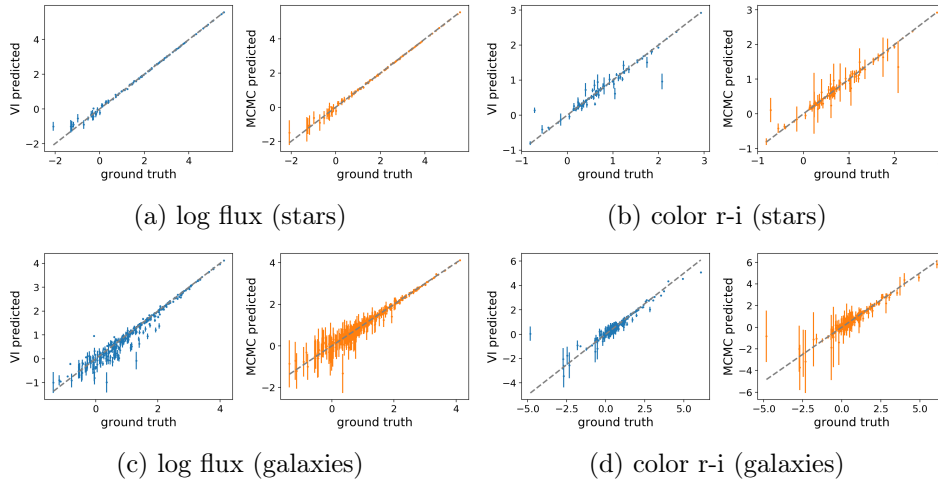


Fig 12: VI and MCMC performance on synthetic data. Each pair depicts VI (left, blue) and MCMC (right, orange) with the ground truth along the  $x$ -axis and the posterior distribution (showing two standard deviations) along the  $y$ -axis.

SDSS images, including the point-spread function  $\psi_n$ , the sky background  $\sigma_n$ , and structural constants like the dimensions of the images. To illustrate that synthetic data resemble real images, Figure 10 depicts a synthetic image generated using parameters from an existing catalog. In our experiments, the light sources in synthetic images are instead drawn from the prior. Our synthetic study set comprises five overlapping  $2048 \times 1489$ -pixel images. Each image is for a different filter band. The images contain approximately 500 detectable light sources.

Empirically, MCMC performs better for star/galaxy classification than VI for all thresholds of a receiver operating characteristic (ROC) curve (Figure 11). Both methods have a high area under the curve (AUC). For MCMC, the AUC is 0.994. For VI, the AUC is 0.981.

Both methods estimate means well for all continuous latent random variables (Table 4). MCMC outperforms VI significantly for some point estimates. “Direction” is error, in arcseconds (0.396 pixels), for the directions of the light sources’ centers. “Flux” measures the reference band (r-band) flux. “Colors” are ratios of magnitudes in consecutive bands. “Galaxy profile” is a proportion indicating whether a galaxy is de Vaucouleurs or exponential. “Galaxy axis” is the ratio between the lengths of a galaxy’s minor and major axes. “Galaxy radius” is the half-light radius of a galaxy in arcseconds. “Galaxy angle” is the orientation of a galaxy in degrees.

For color and flux, MCMC often has larger posterior uncertainty. MCMC assigns substantial probability density to the truth more often than VI (Figure 12). For light sources where posterior means are particularly poor predictors of the truth, VI severely underestimates the uncertainty, whereas MCMC assigns much greater posterior density to the true values (Figure 13). For color and log flux—both normally distributed quantities in this synthetic data—errors from MCMC are more nearly normally distributed than those of VI (Table 5).

These empirical results are anticipated by theory: VI underestimates the posterior uncertainty because independence assumptions in the variational distribution do not hold in the posterior (Bishop 2006). Additionally, dif-

	VI					MCMC			
	within 1/2 sd	1 sd	2 sd	3 sd		within 1/2 sd	1 sd	2 sd	3 sd
log flux	0.18	0.31	0.55	0.68	log flux	0.36	0.64	0.92	0.99
color u-g	0.29	0.52	0.79	0.89	color u-g	0.43	0.73	0.95	1.00
color g-r	0.26	0.46	0.71	0.80	color g-r	0.41	0.68	0.93	0.99
color r-i	0.22	0.43	0.72	0.84	color r-i	0.41	0.67	0.94	0.99
color i-z	0.32	0.58	0.82	0.93	color i-z	0.41	0.71	0.93	0.99

Table 5: Proportion of light sources having posterior means found by VI (left) and MCMC (right) near the ground truth for synthetic images.

ferences between the candidate variational distributions’ marginals and the posteriors’ marginals are a source of bias. For the marginals we approximate with point masses (those of  $u_s$  and  $e_s$ ), that may be a particularly important source of bias.

5.2. *Real images from SDSS.* Absolute truth is not currently knowable for astronomical catalogs. Fortunately, one area of the sky, called “Stripe 82,” has been imaged many times in SDSS. This region provides a convenient validation strategy: combine exposures from all Stripe-82 runs to produce a high signal-to-noise image, then use parameters estimated from the combined exposure as a surrogate ground truth.

Photo (Lupton et al. 2005) is the primary software pipeline for cataloging SDSS. We use Photo’s estimated parameters from the combined Stripe 82 imagery as ground truth. We then run Photo and our method on just one of the 80 image sets, comparing the results from each to the ground truth. Although this “ground truth” is still prone to errors, such errors typically favor Photo, since any systematic errors will be consistent in Photo’s output.

To reduce the runtime of our algorithms, we test them on only a subset of Stripe 82. Our Stripe 82 study set comprises five overlapping  $2048 \times 1489$ -pixel images for a typical region of sky. Each of these images is captured through a different filter. The images contain approximately 500 detectable light sources.

For star/galaxy classification in SDSS data, MCMC outperforms VI at some thresholds and performs slightly worse than VI at others (Figure 14). In addition to point estimates, our inference procedures approximate posterior uncertainty for source type (star or galaxy), flux, and colors. This is a novel feature of a Bayesian approach, offering astronomers a principled measure of the quality of inference for each light source; Photo gives only conditional

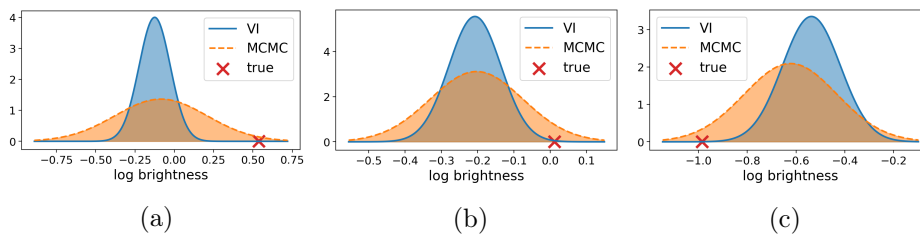


Fig 13: Comparison of posterior uncertainty for the flux of three synthetic light sources where the posterior mean is a poor prediction of the true parameter value. VI underestimates posterior uncertainty. MCMC assigns much greater posterior density to the true values.

uncertainty estimates.

The MCMC procedure is certain ( $> 99\%$  certainty) about the classification (star vs. galaxy) for 321 out of 385 light sources. Of these classifications, 319 (99.4%) are correct. Of the remaining classifications ( $>1\%$  uncertainty), 50 (78.1%) are correct. The VI procedure is certain ( $> 99\%$  certainty) about the classification for 322 out of 385 light sources. Of these classifications, 318 (98.8%) are correct. Of the remaining classifications ( $>1\%$  uncertainty), 53 (84.1%) are correct.

Table 6 is our main empirical result. It quantifies point-estimate error from MCMC and VI for the real-valued latent random variables, as well as providing a paired error comparison between each method. MCMC and VI both substantially outperform Photo. Both make especially large improvements in estimating color. Only our model has a prior on color; Photo estimates band flux independently for each light source.

Point-estimate errors for MCMC and VI differed significantly only for galaxy profile and galaxy axis ratio. For galaxy axis, MCMC outperformed VI, repeating our experience with synthetic data. For galaxy profile, however, VI outperformed MCMC—the opposite of how the methods compared on synthetic data. Sampler diagnostics, though not conclusive, suggest that insufficient mixing was not to blame. Model misfit, though an obvious explanation for any result not shared by synthetic data, seems inadequate because MCMC recovered the other galaxy shape parameters at least as well as VI.

Our leading explanation is that “ground truth” is unreliable for galaxy profile, and that VI more accurately recreates the ground-truth mistakes. Recall ground truth is determined by additively combining many overlapping images. These images were taken through a variety of atmospheric conditions. Errors in the point-spread function (PSF) are likely compounded by the addition of more data. Galaxy profile may be particularly susceptible to errors in the PSF because it has the capacity to model image blur that should have been attributed to the PSF.

For SDSS images, MCMC had better calibrated uncertainty estimates, particularly for log flux (Figure 15, Figure 16, and Table 7). Recall that on the synthetic data, MCMC substantially outperformed VI at modeling uncertainty, producing empirical uncertainties that followed their theoretical distribution almost exactly (Table 5). On real data, uncertainty estimates for both MCMC and VI are worse than on synthetic data. Model misspecification appears to have an effect on MCMC that is comparable to the effect of the bias introduced by the independence assumptions of the variational distribution.

5.3. *Runtime comparison.* MCMC took approximately  $1000\times$  longer in wall-clock time than VI to attain good results. The implementations for

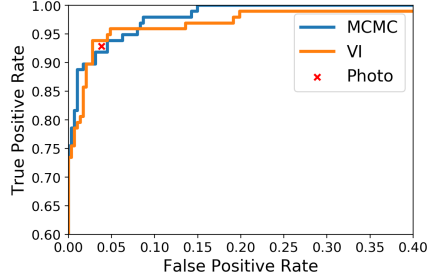


Fig 14: The receiver operating characteristic (ROC) curve for star/galaxy classification on Stripe 82 data. The area under the curve (AUC) for MCMC is 0.991 and for VI is 0.985.

	MCMC	VI	Photo	Photo-VI	Photo-MCMC	VI-MCMC
direction	0.266	0.268	0.271	0.003 ( $\pm$ 0.011)	0.004 ( $\pm$ 0.010)	0.001 ( $\pm$ 0.002)
flux	0.163	0.159	0.168	0.009 ( $\pm$ 0.013)	0.005 ( $\pm$ 0.013)	-0.005 ( $\pm$ 0.008)
color u-g	0.574	0.589	0.943	<b>0.417</b> ( $\pm$ 0.063)	<b>0.428</b> ( $\pm$ 0.063)	0.015 ( $\pm$ 0.008)
color g-r	0.146	0.146	0.293	<b>0.147</b> ( $\pm$ 0.020)	<b>0.147</b> ( $\pm$ 0.019)	0.0005 ( $\pm$ 0.003)
color r-i	0.096	0.097	0.175	<b>0.078</b> ( $\pm$ 0.010)	<b>0.079</b> ( $\pm$ 0.010)	0.001 ( $\pm$ 0.002)
color i-z	0.158	0.153	0.336	<b>0.184</b> ( $\pm$ 0.026)	<b>0.179</b> ( $\pm$ 0.026)	-0.005 ( $\pm$ 0.003)
galaxy profile	0.268	0.195	0.245	<b>0.050</b> ( $\pm$ 0.019)	-0.023 ( $\pm$ 0.018)	<b>-0.073</b> ( $\pm$ 0.015)
galaxy axis	0.115	0.146	0.219	<b>0.073</b> ( $\pm$ 0.012)	<b>0.104</b> ( $\pm$ 0.012)	<b>0.031</b> ( $\pm$ 0.005)
galaxy radius	0.572	0.692	1.274	0.582 ( $\pm$ 0.299)	<b>0.701</b> ( $\pm$ 0.293)	0.120 ( $\pm$ 0.067)
galaxy angle	19.32	19.54	20.39	0.838 ( $\pm$ 1.164)	1.062 ( $\pm$ 1.165)	0.225 ( $\pm$ 0.549)

Table 6: *Left columns:* Mean absolute error on Stripe 82 data. **Lower is better.** *Right columns:* Pairwise error differences for each pair of methods (and standard error). Statistically significant differences appear in bold font.

	VI				MCMC			
	within 1/2 sd	1 sd	2 sd	3 sd	within 1/2 sd	1 sd	2 sd	3 sd
log flux	0.12	0.21	0.39	0.58	0.18	0.37	0.67	0.82
color u-g	0.25	0.44	0.75	0.89	0.30	0.57	0.85	0.91
color g-r	0.25	0.48	0.76	0.91	0.34	0.59	0.85	0.94
color r-i	0.22	0.41	0.72	0.87	0.30	0.58	0.88	0.95
color i-z	0.27	0.51	0.81	0.94	0.33	0.57	0.87	0.95

Table 7: Proportion of light sources having posterior means found by VI (left) and MCMC (right) near the ground truth for SDSS images.

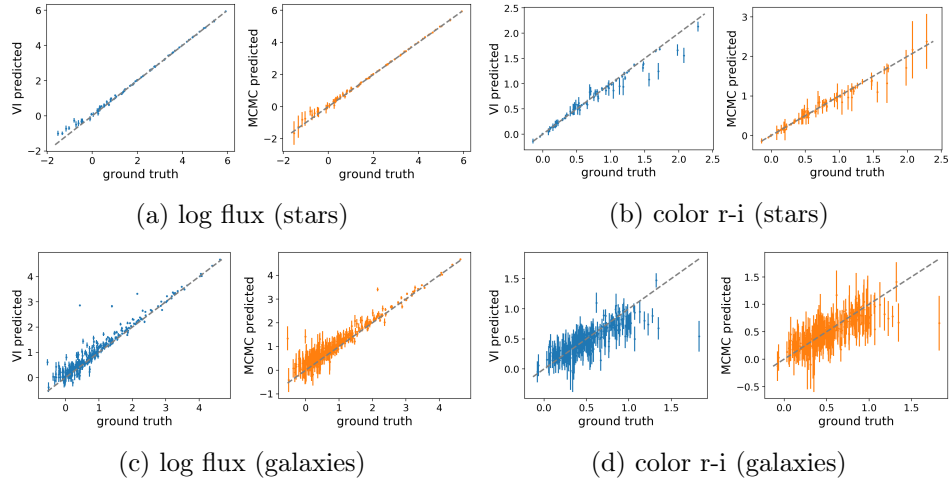


Fig 15: VI and MCMC performance on real data from Stripe 82. Each pair depicts VI (left, blue) and MCMC (right, orange), with the ground truth along the  $x$ -axis and the posterior distribution (showing two standard deviations) along the  $y$ -axis.

MCMC and VI were both carefully optimized for speed, to make their runtimes comparable. In fact, the majority of runtime for MCMC was spent in code also used by VI, since the most computationally intensive calculations (across pixels) are shared by both the variational lower bound and the log likelihood function. This largely rules out “implementation differences” as an explanation for the disparity in runtime.

The same hardware was used for all timing experiments: a single core of an Intel Xeon E5-2698 v3 clocked at 2.30GHz.

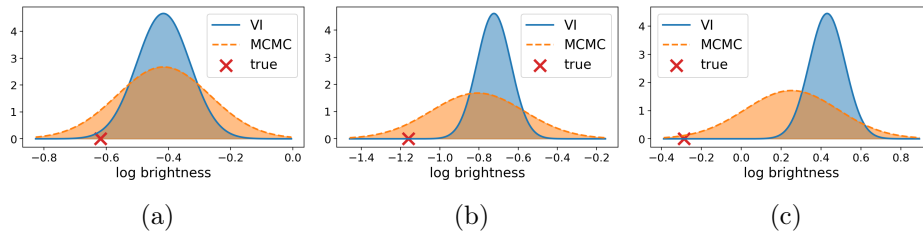
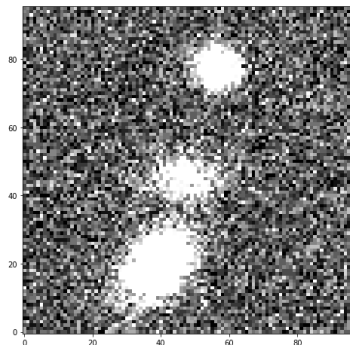
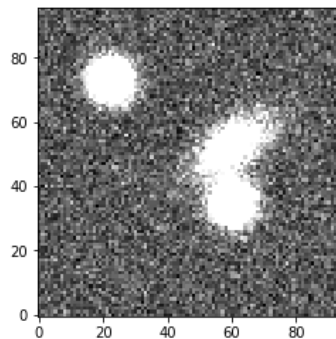


Fig 16: Comparison of posterior uncertainty for the flux of three light sources from Stripe 82 where the posterior mean is a poor prediction of the true parameter value. VI underestimates posterior uncertainty. MCMC assigns much greater posterior density to the true values.





(a) Two galaxies and one star. Their centers are on a line.



(b) Two stars and one galaxy, all having 10-nanomaggy flux density.

Fig 17: Simulated astronomical images from GalSim.

Our MCMC experiments use a temperature schedule of length 200 for annealed importance sampling (AIS). We repeated AIS 25 times to generate 25 independent estimates of the normalizing constant for each model. We then ran each of these 25 independent posterior samples for 25 more slice sampling steps, generating 625 correlated samples. For MCMC, the number of samples drawn scales linearly with runtime, presenting a speed/accuracy trade-off. However, the quality of an MCMC posterior approximation is a function of the number of effectively independent samples (Gelman et al. 2014). We measure the rate at which slice sampling is able to compute effectively independent samples for a single source ( $52 \times 52$  image patch). For stars, we compute 0.225 effectively independent samples per second. For galaxies, we compute 0.138 effectively independent samples per second. VI is able to compute an approximate posterior distribution for one light source in 9 seconds, on average, for a region of sky imaged once in each of five filter bands. This runtime holds for either synthetic or SDSS data; runtime is largely determined by the number of pixels.

5.4. *Deblending.* For the proposed model, overlapping light sources are not a special case requiring special processing logic. Existing cataloging pipelines, on the other hand, invoke specialized “deblending” routines to deal with overlapping light sources, to avoid, for example, double counting photons. In this section, we evaluate our procedure using simulated astronomical images from GalSim (Rowe et al. 2015). Using simulated rather than real data is particularly important for deblending experiments, because ground truth is particularly difficult to establish for overlapping light sources. In contrast to our synthetic data (Section 5.1), the simulated data is not drawn

from our model, so there is the potential for model misfit.

First, we consider images where three or more peaks in a blend appear in a straight line, because this case was the “single biggest failure mode” for the deblending algorithm used by the Hyper Suprime-Cam (HSC) software pipeline (Bosch et al. 2018). To verify that this represents no special challenge to our model, we generated the astronomical image in Figure 17a. The correct r-band fluxes of the light sources, ordered from bottom to top, are 10 nanomaggies, 3 nanomaggies, and 3 nanomaggies. Our VI procedure correctly classifies all three and determines that their respective flux densities are 9.98 nanomaggies, 2.90 nanomaggies, and 3.01 nanomaggies. The classifications are correct (assigning greater than 99% probability to the truth), and mean galaxy angles are both within a few degrees of the truth. We do not report the HSC pipeline’s estimation on this image because we could not get it to run without errors.

Second, we consider images with more severe blending and compare our algorithm to SExtractor (Bertin & Arnouts 1996). Unlike the SDSS and HSC pipelines, SExtractor is relatively straightforward to run on new data. Recently released Python bindings make using it particularly straightforward (Barbary 2016). SExtractor is among the most used cataloging software today.

Figure 17b shows a second simulated image we used for testing. These light sources all have high flux density—10 nanomaggies each. The approximate posterior mean recovered by our VI procedure assigns 9.87 nanomaggies, 9.95 nanomaggies, and 10.12 nanomaggies to these light sources. SExtractor, on the other hand, estimates their flux densities to be 10.85 nanomaggies, 12.81 nanomaggies, and 14.91 nanomaggies.

Melchior et al. (2018) propose a new deblending algorithm, called SCARLET, and report improvements over the HSC approach to deblending. SCARLET appears at first glance to be quite different from our approach: it is based on non-negative matrix factorization (NMF) rather than Bayesian statistics. However, NMF algorithms can be cast as computing a maximum a posteriori (MAP) estimate under some assumptions on the distribution of the data and the factors (Schmidt et al. 2009), so SCARLET may have some similarity to what we propose.

**6. Bayesian inference at petascale.** Catalog inference is a “big data” problem that does not parallelize trivially. This section introduces high-performance computing (HPC) to a statistics audience by describing large-scale runs of our variational inference procedure. We construct a catalog from the entire 50-terabyte SDSS dataset. More importantly, we attain the computational efficiency needed to process the next generation of surveys, which will include  $\mathcal{O}(100)$  petabytes of image data.

6.1. *Hardware.* Our test platform was the Cori supercomputer—currently ranked eighth in the global “Top 500” rankings ([Top500.org 2017](#)). Cori comprises 9,688 compute nodes connected by a high-speed network ([NERSC 2018](#)). Each compute node has 112 GB of memory and one processor, an Intel Xeon Phi 7250, commonly referred to as “Knights Landing.” Though Knights Landing runs at only 1.4 GHz, it more than makes up for this relatively slow clock by executing many instructions in parallel during each clock cycle. A single Knights Landing processor has 68 cores—physically distinct regions of the processor that execute instructions in parallel. Each core simultaneously runs two hardware threads that appear to the operating system as separate cores. A hardware thread executes batches of instructions twice per clock cycle: once on the “up-tick” and once on the “down-tick.” During each tick, a hardware thread may execute the same instruction on eight different 64-byte floating point numbers. This is known as single-instruction multiple-data (SIMD) parallelism.

6.2. *Efficient thread-level execution.* Supercomputer programs are written almost exclusively in verbose languages like assembly, Fortran, C, and C++. Many statisticians, however, prefer very high-level (VHL) languages like R and Python. These languages often require  $5\times$  to  $10\times$  fewer lines of code to express the same algorithm. Unfortunately, they also often run  $10\times$ ,  $100\times$ , or even  $1000\times$  slower than equivalent C code ([Julia developers 2018](#)). For high-performance computing, these languages are therefore limited to serving as “glue” code that connects libraries (e.g., BLAS, TensorFlow) that are implemented in more efficient languages. In turn, writing code in two languages prevents many optimizations ([Bezanson et al. 2017](#)).

Our work uses the Julia programming language ([Bezanson et al. 2017](#)) for the first time in an HPC setting. Julia matches both the succinctness of scripting languages and the speed of C. The “hot spots” in a Julia codebase, however, must be written carefully to attain C-like speed.

The process of tuning Julia code to run in an HPC setting is iterative. It begins with profiling a typical execution of the code to find bottlenecks; intuition about which lines of code are hotspots is a poor substitute for measurement. Our first round of bottlenecks involved memory allocation, where

the program requests that the operating system assign it more memory. We removed all these memory allocations from loops that contributed significantly to runtime by allocating the memory up front (i.e., “pre-allocating” memory).

The next round of bottlenecks was due to memory access: processors cannot execute instructions until data has been transferred from main memory to the processor’s registers. A hardware thread may remain idle for approximately 200 clock cycles while fetching one number from main memory. Memory-access bottlenecks need to be fixed on a case-by-case basis. The solution typically involves some reordering of the computation to enable better prefetching of data from main memory. In some cases, we save time by re-computing values rather than fetching them.

*6.3. Multi-node scaling.* In HPC, “scalability” refers to how a program’s performance varies with the capacity of the hardware devoted to executing the program (Hager & Wellein 2010). We assess scaling empirically in two ways. First, we vary the number of compute nodes while keeping the amount of work constant per compute node (“weak scaling”); many compute nodes can solve a much larger problem. Here the problem size is the area of the sky that we are constructing a catalog for. Second, we vary the number of compute nodes while keeping the total job size constant (“strong scaling”); many compute nodes have to further subdivide the problem. The two scaling metrics give different perspectives to inform predictions about how a particular supercomputer program will perform on future datasets, which may be much larger than any of the datasets used for testing.

Generally, it is harder to use more compute nodes efficiently. Ideal weak scaling is constant runtime as the number of compute nodes increases. Figure 18a shows instead that our runtime roughly doubles as the number of compute nodes increases from 1 to 8192. Ideal strong scaling is runtime that drops by a factor of  $1/c$  when the number of compute nodes grows by a factor of  $c$ . Figure 18b shows instead that our runtime roughly halves as the number of compute nodes quadruples from 2048 to 8192.

Additionally, the scaling graphs break out runtime by component. The *image loading* component is the time taken to load images while worker threads are idle. After the first task, images are prefetched in the background, so the majority of image loading time accrues up front. Image loading time is constant in the weak scaling graph and proportional to the inverse of the number of nodes in the strong scaling graph—exactly what we want. We are not I/O bound even at high node counts.

The *load imbalance* component is time when processes are idle because no tasks remain, but the job has not ended because at least one process has not finished its current task. Both scaling graphs indicate that load imbalance

is our primary scaling bottleneck. Fortunately, the load imbalance is due to having only 4 tasks per process. With at least  $1000\times$  more data, the volume we expect from LSST, the load imbalance should become negligible.

The *task processing* component is the main work loop. It involves no network or disk I/O, only computation and shared memory access. Because of this, task processing serves as a sanity check for both graphs: it should, and does, stay roughly constant in the weak scaling graph and vary in inverse proportion to the number of nodes in the strong scaling graph.

The *other* component is everything else. It is always a small fraction of the total runtime. It includes scheduling overhead, network I/O (excluding image loading), and writing output to disk.

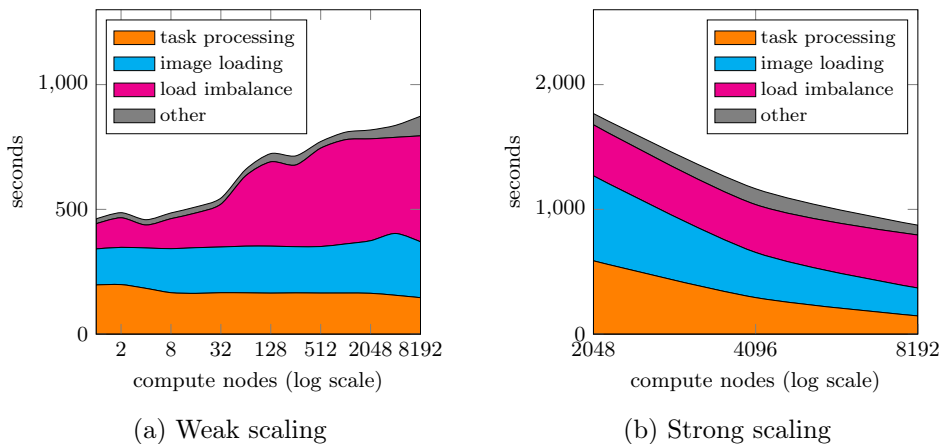


Fig 18: Scaling results. Load imbalance is due to the limited size of our study dataset—real datasets will be much larger. See text for additional discussion.

6.4. *Peak performance.* To assess the peak performance that can be achieved for Bayesian inference at scale, we prepared a specialized configuration for performance measurement in which the processes synchronize after loading images, prior to task processing. We ran this configuration on 9568 Cori Intel Xeon Phi nodes, each running 17 processes of eight threads each, for a total of 1,303,832 threads. 57.8 TB of SDSS image data was loaded over a ten-minute interval. (Some regions were loaded multiple times, as prescribed by our algorithm.) The peak performance achieved was 1.54 PFLOP/s in double-precision. To the best of our knowledge, this experiment (conducted in May 2017) was the first time a supercomputer program in any language other than C, C++, Fortran, or assembly has exceeded one petaflop in double-precision.

6.5. *Complete SDSS catalog.* In a long-running job with 256 compute nodes, we constructed a preliminary astronomical catalog based on the entire SDSS. The catalog is 21 GB and contains 112 million light sources. Spot checking results gives us high confidence that distributed executions of our program give the same results as serial executions. We are considering both the FITS file format (Wells & Greisen 1979) and the HDF5 file format (Folk et al. 2011) for distributing future catalogs. FITS is the standard format for astronomical images and catalogs, whereas the HDF5 format has better I/O speed and compression (Price et al. 2015). Another possibility is distributing the catalog inference code rather than the catalog. That approach encourages users to adapt the statistical model and the priors to their needs and to treat the catalog as an intermediate data product (Turon et al. 2010).

6.6. *How to use a Bayesian catalog.* Catalogs based on approximate posterior inference need to be used differently than traditional catalogs, which are based on frequentist statistics. Loredo (2007) and Loredo & Hendry (2010) introduce Bayesian statistics for astronomy. Posterior means and medians minimize  $L_2$  and  $L_1$  error, respectively, but both point estimates are biased in general for individual light sources. For population-level analysis, in Bayesian statistics, queries are typically addressed by integrating the (approximate) posterior to compute marginal distributions. Integrating may be analytic in some cases for VI. Monte Carlo integration is more universally applicable; that is, drawing samples from the (approximate) posterior and computing statistics on their empirical distribution. Given access to marginal distributions, hypothesis testing amounts to computing a Bayes factor (Held & Ott 2018, Loredo 2007).

6.7. *Future hardware.* In July, 2018, it was reported that Intel will discontinue development of the Xeon Phi line of processors (Morgan 2018). Future supercomputers will likely be based instead on the Xeon Scalable Family line of processors (Mujtaba 2018) and the AMD Epyc (Smith 2018). Both are “many core” processors having tens of cores, like the Xeon Phi, but they are clocked at a higher rate. Running efficiently on these processors should not require significant changes to our algorithm or to our Julia implementation. The Julia compiler and LLVM, on the other hand, may require optimizations to fully exploit the capabilities of these processors.

The next generation of supercomputers may also rely more on GPUs to attain exascale performance (Feldman 2018). The variable size of imaged light sources makes SIMD parallelization across light sources somewhat challenging. A different approach to parallelization may be advisable for astronomical cataloging on GPU-based clusters.

**7. Discussion.** We introduced our work by identifying a limitation of existing cataloging pipelines: centroiding, deblending, photometry, star/galaxy separation, and incorporation of priors happen in distinct stages. Uncertainty is typically not propagated between stages. Any uncertainty estimates these pipelines produce are based on conditional distributions—that is, they are conditional on the output of the previous stages.

We developed a joint model of light sources’ centers, colors, fluxes, shapes, and types (star/galaxy). Whereas previous approaches to cataloging have been framed in algorithmic terms, statistical formalisms let us characterize our inferences without ambiguity. Statistical formalisms also make modeling assumptions relatively transparent—whether the assumptions are appropriate ultimately depends on the downstream application. We highlighted limitations of the model to guide further development.

A model is only useful when it can be applied to data. We proposed two procedures: one based on MCMC and the other on VI. Neither MCMC nor VI could be applied to our model without customization. The need for problem-specific adjustments is a barrier to the broader adoption of both techniques. With MCMC, for example, we went through several iterations before settling on slice sampling and AIS, including Metropolis-Hastings (MH) and reversible jump (Green 1995). Compared to slice sampling, we found MH difficult to tune. We found that reversible-jump MCMC required carefully constructed proposals to jump often enough between the star and galaxy models and was also difficult to tune.

VI required even more problem-specific customization. Our VI techniques include the following: 1) approximating an integrand with its second-order Taylor expansion; 2) approximating the point-spread function with a mixture of Gaussians; 3) upper bounding the KL divergence between the color and a GMM prior; 4) limiting the variational distribution to a structured mean-field form; 5) limiting the variational distribution to point masses for some parameters; and 6) optimizing the variational lower bound with a variant of Newton’s method rather than coordinate ascent. This final technique was particularly laborious, as it involved manually deriving and implementing both gradients and Hessians for a complicated function.

On synthetic data, MCMC was better at quantifying uncertainty, which is likely due to the restrictive form of the variational distribution. Additionally, MCMC provided uncertainty estimates for all latent random variables, whereas VI modeled some random variables as point masses—in effect recovering maximum a posteriori (MAP) estimates for them. However, MCMC was approximately  $1000\times$  slower than VI.

On real data, while both inference procedures’ point estimates were better than current standard practice, neither procedures’ uncertainty estimates

were well calibrated, particularly for galaxies. Uncalibrated uncertainties can nonetheless be useful, e.g., for flagging particularly unreliable point estimates. Additionally, even if the uncertainties are ignored by downstream analyses, point estimates typically improve when ambiguity is modeled.

Uncertainty quantification may be particularly susceptible to model misspecification. For questions requiring calibrated uncertainties, enhancing the galaxy model may help to reduce model misspecification. Though the galaxy model we use—one with elliptical contours—is standard in astronomy, a more flexible galaxy model shows promise (Regier et al. 2015).

Because astronomical surveys are large (comprising terabytes of data now, and petabytes in the near future), scalability is of paramount concern. We approximated the posterior for a large image dataset and demonstrated the scaling characteristics necessary to apply approximate Bayesian inference to hundreds of petabytes of images from the next generation of astronomical surveys. Our optimization procedure found a stationary point, even though doing so required treating the full dataset as a single optimization problem.

Because of the relative ease of deriving and implementing MCMC, it could be a useful tool for trying different models and testing for misspecification prior to implementing VI. In some cases, it may be simpler to expend more computational resources to scale up the MCMC procedure than to implement VI. For the most computationally intensive problems, however, only VI can currently perform approximate inference.



## SUPPLEMENTARY MATERIAL

**Supplement A: Kullback-Leibler divergences**

(; kl.pdf). Formulas for KL divergences between common distributions that appear in the derivation of the variational lower bound.

**References.**

- Barbary, K. (2016), ‘SEP: Source Extractor as a library’, *The Journal of Open Source Software* **1**(6), 59.
- Bertin, E. & Arnouts, S. (1996), ‘SExtractor: Software for source extraction’, *Astronomy and Astrophysics Supplement Series* **117**(2), 393–404.
- Bezanson, J., Edelman, A., Karpinski, S. & Shah, V. B. (2017), ‘Julia: A fresh approach to numerical computing’, *SIAM Review* **59**(1).
- Bickel, P. J. & Doksum, K. A. (2015), *Mathematical Statistics: Basic Ideas and Selected Topics*, Vol. 1, 2 edn, CRC Press, chapter 5.
- Bishop, C. (2006), *Pattern Recognition and Machine Learning*, Springer, New York, NY.
- Blei, D. M., Kucukelbir, A. & McAuliffe, J. D. (2017), ‘Variational inference: A review for statisticians’, *Journal of the American Statistical Association* **112**(518), 859–877.
- Bosch, J., Armstrong, R., Bickerton, S. et al. (2018), ‘The Hyper Suprime-Cam software pipeline’, *Publications of the Astronomical Society of Japan* **70**.
- Brewer, B. J., Foreman-Mackey, D. & Hogg, D. W. (2013), ‘Probabilistic catalogs for crowded stellar fields’, *The Astronomical Journal* **146**(1).
- Bubeck, S. (2015), ‘Convex optimization: Algorithms and complexity’, *Foundations and Trends in Machine Learning* **8**(3-4).
- Doi, M., Tanaka, M. et al. (2010), ‘Photometric response functions of the Sloan Digital Sky Survey imager’, *The Astronomical Journal* **139**(4).
- Fan, Y. & Sisson, S. A. (2011), ‘Reversible jump Markov chain Monte Carlo’, *Handbook of Markov Chain Monte Carlo*.
- Feigelson, E. D. & Babu, G. J. (2012), *Modern Statistical Methods for Astronomy: With R Applications*, Cambridge University Press, Cambridge, UK.
- Feldman, M. (2018), ‘Summit up and running at Oak Ridge’, <https://www.top500.org/news/summit-up-and-running-at-oak-ridge-claims-first-exascale-application/>. [Online; accessed August 20, 2018].
- Folk, M., Heber, G., Koziol, Q., Pourmal, E. & Robinson, D. (2011), An overview of the HDF5 technology suite and its applications, in ‘Proceedings of the EDBT/ICDT 2011 Workshop on Array Databases’, pp. 36–47.
- Fraysse, A. & Rodet, T. (2014), ‘A measure-theoretic variational Bayesian algorithm for large dimensional problems’, *SIAM Journal on Imaging Sciences* **7**(4).
- Friel, N. & Wyse, J. (2012), ‘Estimating the evidence—a review’, *Statistica Neerlandica* **66**(3).
- Fukugita, M., Ichikawa, T., Gunn, J. E., Doi, M., Shimasaku, K. & Schneider, D. P. (1996), ‘The Sloan Digital Sky Survey photometric system’, *The Astronomical Journal* **111**.
- Gelman, A., Carlin, J. B., Stern, H. S., Dunson, D. B., Vehtari, A. & Rubin, D. B. (2014), Basics of Markov chain simulation, in ‘Bayesian Data Analysis’, Vol. 3, CRC Press, chapter 11.
- Gelman, A. & Rubin, D. B. (1992), ‘Inference from iterative simulation using multiple sequences’, *Statistical Science* **7**(4), 457–472.
- Giordano, R. J., Broderick, T. & Jordan, M. I. (2015), Linear response methods for accurate covariance estimates from mean field variational bayes, in ‘Advances in Neural Information Processing Systems’, pp. 1441–1449.

- Green, P. J. (1995), ‘Reversible jump Markov chain Monte Carlo computation and Bayesian model determination’, *Biometrika* **82**(4), 711–732.
- Greisen, E. W. & Calabretta, M. R. (2002), ‘Representations of world coordinates in FITS’, *Astronomy & Astrophysics* **395**(3).
- Hager, G. & Wellein, G. (2010), *Introduction to High Performance Computing for Scientists and Engineers*, CRC Press, Boca Raton, FL.
- Held, L. & Ott, M. (2018), ‘On p-values and Bayes factors’, *Annual Review of Statistics and Its Application* **5**(1).
- Hershey, J. R. & Olsen, P. A. (2007), Approximating the Kullback Leibler divergence between Gaussian mixture models, in ‘IEEE International Conference on Acoustics, Speech and Signal Processing’, Vol. 4, pp. 317–320.
- Julia developers (2018), ‘Julia micro-benchmarks’, <https://julialang.org/benchmarks/>. [Online; accessed January 23, 2018].
- Lang, D., Hogg, D. W. & Mykytyn, D. (2016), ‘The Tractor: Probabilistic astronomical source detection and measurement’, Astrophysics Source Code Library.
- Loredo, T. J. (2007), Analyzing data from astronomical surveys: Issues and directions, in ‘Statistical Challenges in Modern Astronomy IV’, Vol. 371.
- Loredo, T. J. & Hendry, M. A. (2010), Bayesian multilevel modelling of cosmological populations, in ‘Bayesian Methods in Cosmology’, Cambridge University Press, New York.
- LSST (2017), ‘About LSST’, <http://www.lsst.org/about>. [Online; accessed September 12, 2017].
- Lupton, R., Gunn, J. E., Ivezić, Z., Knapp, G. R. & Kent, S. (2001), The SDSS imaging pipelines, in F. R. Harnden, Jr., F. A. Primini & H. E. Payne, eds, ‘Astronomical Data Analysis Software and Systems X’, Vol. 238 of *Astronomical Society of the Pacific Conference Series*, pp. 269–280.
- Lupton, R. H., Ivezić, Z. et al. (2005), SDSS image processing II: The photo pipelines, Technical report, Princeton University. preprint at <https://www.astro.princeton.edu/~rhl/photo-lite.pdf>.
- MacKay, D. J. (1995), Developments in probabilistic modelling with neural networks—ensemble learning, in ‘Neural Networks: Artificial Intelligence and Industrial Applications’, Springer.
- Melchior, P., Moolekamp, F., Jerdee, M., Armstrong, R., Sun, A.-L., Bosch, J. & Lupton, R. (2018), ‘SCARLET: Source separation in multi-band images by constrained matrix factorization’, *arXiv:1802.10157*.
- Morgan, T. (2018), ‘The end of Xeon Phi’, <https://www.nextplatform.com/2018/07/27/end-of-the-line-for-xeon-phi-its-all-xeon-from-here/>. [Online; accessed August 20, 2018].
- Mujtaba, H. (2018), ‘Intel Xeon Scalable Family roadmap revealed’, <https://wccftech.com/intel-xeon-scalable-family-roadmap-revealed-points-out-cascade-lake-sp-in-q4-2018-cooper-lake-sp-in-q4-2019-ice-lake-sp-in-1h-2020/>. [Online; accessed August 20, 2018].
- Murphy, K. (2012), *Machine Learning: A Probabilistic Perspective*, MIT Press, Cambridge, MA.
- Neal, R. M. (2001), ‘Annealed importance sampling’, *Statistics and Computing* **11**(2), 125–139.
- Neal, R. M. (2003), ‘Slice sampling’, *The Annals of Statistics* **31**(3), 705–741.
- NERSC (2018), ‘Cori configuration’, <http://www.nersc.gov/users/computational-systems/cori/configuration/>. [Online; accessed January 23, 2018].
- Nocedal, J. (2006), *Numerical Optimization*, Springer, New York, NY.
- Portillo, S. K. N., Lee, B. C. G., Daylan, T. & Finkbeiner, D. P. (2017), ‘Improved point-

- source detection in crowded fields using probabilistic cataloging’, *The Astronomical Journal* **154**(4).
- Price, D., Barsdell, B. & Greenhill, L. (2015), ‘HDFITS: Porting the FITS data model to HDF5’, *Astronomy and Computing* **12**.
- Regier, J., McAuliffe, J. & Prabhat (2015), ‘A deep generative model for astronomical images of galaxies’, *NIPS Workshop: Advances in Approximate Bayesian Inference*.
- Rowe, B., Jarvis, M., Mandelbaum, R., Bernstein, G. M., Bosch, J., Simet, M., Meyers, J. E., Kacprzak, T., Nakajima, R., Zuntz, J. et al. (2015), ‘GALSIM: The modular galaxy image simulation toolkit’, *Astronomy and Computing* **10**.
- Schmidt, M. N., Winther, O. & Hansen, L. K. (2009), Bayesian non-negative matrix factorization, in ‘International Conference on Independent Component Analysis and Signal Separation’, pp. 540–547.
- SDSS (2017), ‘Measures of flux and magnitude’, <http://www.sdss3.org/dr8/algorithms/magnitudes.php>. [Online; accessed November 12, 2017].
- SDSS (2018a), ‘Camera’, <http://www.sdss.org/instruments/camera/>. [Online; accessed January 30, 2018].
- SDSS (2018b), ‘Data model: frame’, [https://data.sdss.org/datamodel/files/BOSS\\_PHOTOOBJ/frames/RERUN/RUN/CAMCOL/frame.html](https://data.sdss.org/datamodel/files/BOSS_PHOTOOBJ/frames/RERUN/RUN/CAMCOL/frame.html). [Online; accessed August 21, 2018].
- SDSS (2018c), ‘Glossary of SDSS-IV terminology’, <https://www.sdss.org/dr14/help/glossary/#N>. [Online; accessed August 21, 2018].
- SDSS (2018d), ‘Sky coverage’, <http://classic.sdss.org/dr7/coverage/>. [Online; accessed January 30, 2018].
- Skilling, J. (2004), Nested sampling, in ‘American Institute of Physics Conference Series’, Vol. 735, pp. 395–405.
- Šmídl, V. & Quinn, A. (2006), *The Variational Bayes Method in Signal Processing*, Springer, New York, NY.
- Smith, R. (2018), ‘AMD reaffirms 7nm Epyc Rome server processors sampling in 2H 2018’, <https://www.anandtech.com/show/13122/amd-rome-epyc-cpus-to-be-fabbed-by-tsmc>. [Online; accessed August 20, 2018].
- Top500.org (2017), ‘Top500 list – November 2017’, <http://www.top500.org/list/2017/11/>. [Online; accessed November 16, 2017].
- Turon, C., Meynadier, F., Arenou, F., Hogg, D. & Lang, D. (2010), ‘Telescopes don’t make catalogues!’, *European Astronomical Society Publications Series* **45**.
- van Leeuwen, D. (2018), ‘GaussianMixtures.jl’, <https://github.com/davidavdav/GaussianMixtures.jl>. [Online; accessed August 21, 2018].
- Wells, D. C. & Greisen, E. W. (1979), FITS—a flexible image transport system, in ‘Image Processing in Astronomy’, pp. 445–471.
- Zheng, Y., Fraysse, A. & Rodet, T. (2015), ‘Efficient variational Bayesian approximation method based on subspace optimization’, *IEEE Transactions on Image Processing* **24**(2).

**Supplement A: Kullback-Leibler divergences.** This section gives the formulas for common Kullback-Leibler divergences that appear in the derivation of variational lower bound.

The KL divergence for  $a_s$  is between two categorical distributions.

$$(43) \quad D_{\text{KL}}(q(a_s), p(a_s)) = \acute{a}_s \log \frac{\acute{a}_s}{\mathcal{A}} + (1 - \acute{a}_s) \log \frac{1 - \acute{a}_s}{1 - \mathcal{A}}$$

The KL divergence for  $u_s$  is between a point mass and a uniform distribution.

$$(44) \quad D_{\text{KL}}(q(u_s), p(u_s)) = \frac{1}{360 \times 180}$$

The KL divergence for  $e_s^{\text{angle}}$  is between a point mass and a uniform distribution.

$$(45) \quad D_{\text{KL}}(q(e_s^{\text{angle}}), p(e_s^{\text{angle}})) = \frac{1}{180}$$

The KL divergence for  $e_s^{\text{radius}}$  is between a point mass and a log-normal distribution.

$$(46) \quad D_{\text{KL}}(q(e_s^{\text{radius}}), p(e_s^{\text{radius}})) = -\log 2\pi - \frac{1}{2} \log \mathcal{E}_2^{\text{radius}} - \frac{(e_s^{\text{radius}} - \mathcal{E}_1^{\text{radius}})^2}{2\mathcal{E}_2^{\text{radius}}}$$

The KL divergence for  $e_s^{\text{profile}}$  is between a point mass and a Beta distribution. Here  $B$  denotes the beta function.

$$(47) \quad D_{\text{KL}}(q(e_s^{\text{profile}}), p(e_s^{\text{profile}})) = (\mathcal{E}_1^{\text{profile}} - 1) \log \acute{e}_s^{\text{profile}} + (\mathcal{E}_2^{\text{profile}} - 1) \log(1 - \acute{e}_s^{\text{profile}}) - B(\mathcal{E}_1^{\text{profile}}, \mathcal{E}_2^{\text{profile}})$$

The KL divergence for  $e_s^{\text{axis}}$  is between a point mass and a Beta distribution.

$$(48) \quad D_{\text{KL}}(q(e_s^{\text{axis}}), p(e_s^{\text{axis}})) = (\mathcal{E}_1^{\text{axis}} - 1) \log \acute{e}_s^{\text{axis}} + (\mathcal{E}_2^{\text{axis}} - 1) \log(1 - \acute{e}_s^{\text{axis}}) - B(\mathcal{E}_1^{\text{axis}}, \mathcal{E}_2^{\text{axis}})$$

The KL divergence for  $r_s^{\text{axis}}$  is between two log-normal distributions.

$$(49) \quad D_{\text{KL}}(q(r_s|a_s = i), p(r_s|a_s = i)) = \log \frac{\mathcal{R}_{i2}}{\hat{r}_{si}} + \frac{\hat{r}_{si} + (\hat{r}_{si} - \mathcal{R}_{i1})^2}{2\mathcal{R}_{i2}} - \frac{1}{2}$$

JEFFREY REGIER  
DEPARTMENT OF ELECTRICAL ENGINEERING  
AND COMPUTER SCIENCES  
UNIVERSITY OF CALIFORNIA, BERKELEY  
465 SODA HALL  
BERKELEY, CA 94720  
USA  
E-MAIL: [jregier@eecs.berkeley.edu](mailto:jregier@eecs.berkeley.edu)

DAVID SCHLEGEL  
LAWRENCE BERKELEY NATIONAL LABORATORY  
1 CYCLOTRON ROAD  
BERKELEY, CA 94720  
USA  
E-MAIL: [djschlegel@lbl.gov](mailto:djschlegel@lbl.gov)

JON D. McAULIFFE  
DEPARTMENT OF STATISTICS  
UNIVERSITY OF CALIFORNIA, BERKELEY  
367 EVANS HALL  
BERKELEY, CA 94720  
USA  
E-MAIL: [jon@stat.berkeley.edu](mailto:jon@stat.berkeley.edu)

ANDREW C. MILLER  
SCHOOL OF ENGINEERING  
AND APPLIED SCIENCES  
HARVARD UNIVERSITY  
29 OXFORD STREET  
CAMBRIDGE, MA 02138  
USA  
E-MAIL: [acm@seas.harvard.edu](mailto:acm@seas.harvard.edu)

RYAN P. ADAMS  
PRINCETON UNIVERSITY  
DEPARTMENT OF COMPUTER SCIENCE  
35 OLDEN STREET  
PRINCETON, NJ 08540  
USA  
E-MAIL: [rpa@princeton.edu](mailto:rpa@princeton.edu)

PRABHAT  
LAWRENCE BERKELEY NATIONAL LABORATORY  
1 CYCLOTRON ROAD  
BERKELEY, CA 94720  
USA  
E-MAIL: [prabhat@lbl.gov](mailto:prabhat@lbl.gov)